UNIVERSIDADE FEDERAL DO RIO GRANDE DO SUL
INSTITUTO DE INFORMÁTICA
CURSO DE BACHARELADO EM CIÊNCIA DA COMPUTAÇÃO

RENATO OLIVEIRA DA SILVA

In-line holographic microscopy setup analysis by numerical reconstruction of recorded and modeled holograms

Undergraduate Thesis presented in partial fulfillment of the requirements for the degree of Bachelor of Computer Science

Prof. Dr.
Manuel Menezes de Oliveira Neto
Advisor

Porto Alegre, November 2010

CONTENTS

LIST OF FIGURES

LIST OF TABLES

ABSTRACT

Digital in-line holographic microscopy setups are being used in several applications. The available literature has presented much theoretical information on the resolution limit one can achieve. However, it is still not clear how all the parameters interact with each other in terms of reconstruction quality. This matter is addressed in this work by the use of algorithms for numerical modeling and reconstruction of in-line holograms.

A visual comparison of simulated setups with widely available sensors and laser wavelengths is made, and important attributes are pointed out. The direct use of the divergent emission of a low-cost laser diode is proposed, in contrast of the use of pinhole or lenses, to form, to the best of my knowledge, the simplest realization of in-line holographic setups. This feature enables that extremely simple arrangements, formed by just a sensor camera and the laser diode, can perform the recording of the holograms with moderate results on the reconstruction quality.

Results of this analysis is presented along with examples of reconstructed images of holograms from the numerical modeling algorithm and from real setups based on digital camera and cell phone sensor.

Análise de *setups* de microscopia holográfica *in-line* por reconstrução numérica de hologramas capturados e modelados

RESUMO

Microscopia holográfica *in-line* digital está sendo usada em uma variadade de aplicações. A literatura disponível apresentou muita informação teórica sobre os limites de resolução que se pode atingir. No entanto, ainda não é claro como os parâmetros interagem entre si em termos de qualidade de reconstrução. Essa questão é tratada neste trabalho através do uso de algoritmos de modelagem e reconstrução numérica de hologramas *in-line*.

Uma comparação visual de *setups* simulados com sensores e lasers de comprimentos de onda largamente disponíveis é feita, e atributos importantes são apontados. O uso direto da emissão divergente de um diodo laser de baixo custo é proposto, em contraste com o uso de um microfuro ou lentes, para formar, tanto quanto é do meu conhecimento, a realização mais simples de uma configuração holográfica in-line. Essa característica possibilita que *setups* extremamente simples, formados apenas por um sensor de câmera digital e um diodo laser, possam registrar hologramas com resultados moderados na qualidade de reconstrução.

Os resultados dessa análise são apresentados assim como exemplos de images reconstruídas tanto de hologramas modelados numericamente pelo algoritmo como capturados por *setups* reais baseados em sensores de câmeras digital e de celular.

Palavras-chave: Holografia, Microscopia, Simulação Numérica, Laser.

GLOSSARY

- CCD - Charge-Coupled Device - Common type of sensor in digital cameras.

- CMOS - Complementary Metal-Oxide-Semiconductor - Common type of sensor in digital cameras.

- DIHM - Digital In-Line Holographic Microscopy

- DSLR - Digital Single-Lens Reflex - Class of cameras that, among other features, has bigger sensor sizes than the most common cameras and accepts interchangeable lenses.

- FFT - Fast Fourier Transform

- NA - Numerical aperture - Represents the ranges of angles that an optical system can accept or emit relative to a point position.

1 INTRODUCTION

Reconstruction of wavefronts as a means for microscopy imaging was the very inspiration of Gabor (GABOR, 1948) to present the new process of holography. His initial in-line arrangement is still being used for its simplicity and great results. The concept of recording three-dimensional information about an object is still being explored in a wide range of applications and is particularly interesting in the context of microscopy, for one can reconstruct arbitrary focus planes in a single captured image of a sample, in contrast to ordinary optical microscopy where the depth of field is very thin and limits the information that can be extracted at a given instant or captured image. However, Gabor's experiments suffered from the lack of coherent illumination source and efficient recording processes. His arrangement is sometimes referred in the literature as in-line holography.

With the invention of the laser, much more attention was given to process of holography in diverse applications. More recently, with the widespread use of digital sensors such as CCD and CMOS chips, numerical reconstruction of wavefronts have become available and because laser sources are also getting widely available at lower cost, good quality with particularly simple setups can be easily achieved. Without the use of any optical elements such as expensive lenses, one can record fields of microscopic structures.

Resolution concerns have been discussed in the available literature, theoretical limits have been established and parameters such as the numerical aperture and laser wavelength have been pointed as having fundamental effects on reconstruction resolution. However, it is not clear what kind of quality and possibilities one can achieve with a given setup. This concern is addressed in this work, which compares several parameters of in-line holographic setups for microscopy, and clearly shows how they affect the final reconstruction of the original objects.

With digital sensors growing in quality and having progressively lower costs, attention is turned to the question of what kind of results one can achieve with extremely low cost sensors such as the ones on low-cost phones and webcams. Likewise, with the wide availability of laser diodes in the form of laser pointers, particularly in the red wavelength range (i.e. about 650nm) which are extremely low cost, it remains to be assessed what results can be observed.

Furthermore, laser diodes have an interesting feature which is the naturally divergent nature of its point-like source of illumination that is usually collimated with a special lens in laser pointers. This feature is explored in this work to be, to the best of my knowledge, the simplest realization of an in-line holographic microscope yet. Limitations and considerations of the use of this kind of radiation source are discussed in this work.

Images of real captured data with the proposed setup are provided along with reconstructed planes. In a similar fashion, parameters of these setups are discussed and compared to the modeled results, as to clearly identify what are their effects on the final

reconstructed result.

Due to the multidisciplinary nature of this work, the following chapter explains some basic concepts for the general understanding of how the holographic process work, with no mathematical details. However, in chapter 4 detailed mathematical aspects of the numerical realization of related techniques are presented in order to define the computed results.

1.1 Structure of this work

The remaining of this work is organized as follows: Chapter 2 introduces basic concepts for the understanding of the principles of holography and achievable resolution in in-line holographic microscopy; Chapter 3 discusses related work; Chapter 4 presents implementation details of both algorithms used in this work; Chapter 5 discusses experimental concerns; Chapter 6 presents an analysis of the involved parameters through the reconstruction of modeled and experimentally recorded holograms; Finally, Chapter 7 summarizes this work and presents some future work possibilities.

2 BASIC CONCEPTS

2.1 Holography

Holography is an imaging process that addresses the fundamental problem of recording, and later reconstructing, both the amplitude and the phase of optical wavefronts arriving from a coherently illuminated object. This process is an ingenious way of combining two phenomena that arise from the wave nature of light: namely *interference* and *diffraction*. This is accomplished by two distinct operations of a recording step and a reconstruction step.

A *wavefront* is the set of points in a wave that have the same phase and defines a surface in three dimensions. Wavefronts interfere with each other when they meet at a point in time and space, as illustrated in Figure 2.1. They also exhibit diffraction phenomena when they meet obstacles, as illustrated in Figure 2.3.

2.1.1 Wavefront recording

The recording step comprises techniques to address the problem of recording both amplitude and phase information on recording media or sensors that respond only to light intensity (meaning unable to directly record phase information), such as photographic plates or image sensors —referred simply as the *screen* or *sensor* from now on. This is done through a technique called interferometry, in which the unknown wavefront is added together to a second and mutually coherent wavefront of known amplitude and phase (GOODMAN, 2004). The unknown wavefront will be referred as the "object wave" and the known wavefront as "reference wave".

Two wavefronts are coherent when their phase difference remains constant over time. Coherent wavefronts produce well defined holographic patterns, whereas low coherent wavefronts will average the interference which may not produce a pattern at all. In holog-

Constructive interference   Destructive interference
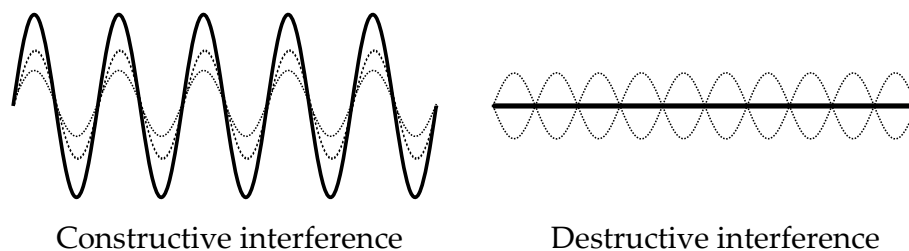
Figure 2.1: Constructive interference of two in-phase waves and destructive interference of two out-of-phase waves. Solid lines represent the wave resulting from the interference of the two dotted waves in each example.

(a) Non-coherent wave-
fronts

(b) Coherent wavefronts
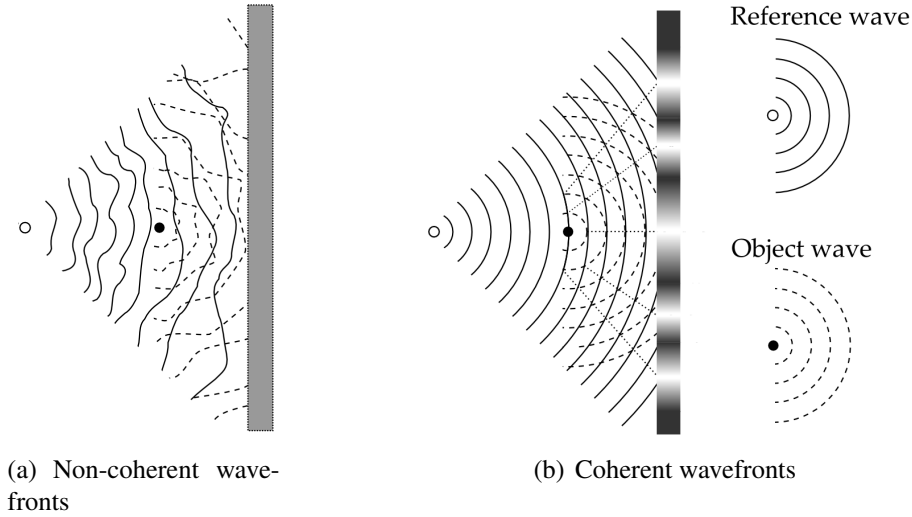
Figure 2.2: Illustration of holographic recording attempts of a diffracting particle. (a) depicts how random non-coherent wavefronts average the interferences on the sensor over time, while in (b) coherent wavefronts tend to interfere continuously at the same positions over time, producing well-defined holographic patterns. The straight dotted lines in (b) are marking the points of in-phase interference of the wavefronts. The white circles represent light sources, while the black circles represent small particles.

raphy one uses highly coherent light emission such as a laser to interfere with itself at another point. Figure 2.2 illustrates this concept by depicting holographic recording attempts on incoherent and coherent illumination.

Because of the wave nature of light, the two coherent wavefronts will interfere when superposed on the screen. The phases of the two wavefronts on the screen will define the recorded intensity at each point on the screen, with constructive and destructive interferences relating to bright and dark intensities, respectively, as seen in Figure 2.2(b). The recorded intensities of the interference pattern on the screen is called a *hologram*. The hologram contains encoded phase information in its holographic patterns, which is then retrieved at the reconstruction step.

2.1.2 Reconstruction of the wavefront

The reconstruction step comprises techniques to address the problem of reconstructing the object wave with the reference wave. This is optically done by illuminating the recorded hologram with the reference wave, which will, by means of diffraction on the hologram, reconstruct two images of the object wave. Figure 2.3 illustrates how diffraction can bend a wavefront at an obstacle. When the screen is an image sensor, the reconstruction step is done numerically by a computer and the technique is called *digital holography*.

In traditional holography, the original wavefront of the object is reconstructed by illuminating the hologram with the reference used to record it. The effect is that one can look into the hologram plate like a window to the object wavefront and will experience depth-related properties like parallax and depth-of-field (KREIS, 2005). For digital holography, the reconstruction of the object wavefront can be numerically calculated by a similar approach by calculating the diffraction of a known wave at the aperture of the recorded hologram. This can be done using the Kirchhoff-Helmholtz diffraction integral (BARTON,

Huygens's Principle   Diffraction Model
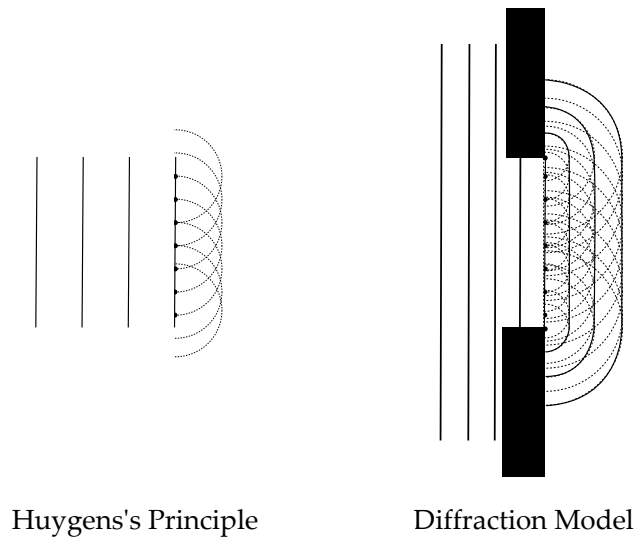
Figure 2.3: Huygens's principle of waves and diffraction model at an aperture illustrating the bending of the wavefront. Lightly shaded arcs depicts Huygens's concept of infinite point sources at each wavefront, while the heavy lines represent the wavefronts.

1988; KREUZER et al., 1992; GARCIA-SUCERQUIA et al., 2006) which expresses the value of the wavefront at a point of observation in terms of the disturbance values at the aperture (i.e. the recorded hologram).

Reconstruction of the wavefront by illuminating or numerically propagating a reference wave through the hologram produces simultaneously a real and a virtual image. If we consider a point object, the real image belongs to a wavefront converging to a focus and the virtual image belongs to a diverging wave from a point. Both these waves are located symmetrically about the hologram plane at the same distance from it as the original object, and are so similar they are called twin images. In the reconstructed wavefront both images can be seen but at different distances and locations.

In traditional *in-line holography*, where the elements of the holographic system are placed in one optical axis, these twins images were a problem when reconstructing the object wavefront because in this setup the reconstructed wave has the two images superposed in the same optical axis, although separated in distance from the hologram. Therefore, when one focuses at one of the images of the reconstructed wavefront, the other image appears unfocused near the first, thus reducing the image quality of the reconstruction. This problem was later avoided by the use of off-axis setups, which focus on effectively separating the images by introducing an angle between the reference and the object waves.

However, while it is true that the twin images are an issue in in-line holographic microscopes, where the source-object distance is of the same order of the expected resolution of the method, this is not the case in the setup used in this work. It has been demonstrated in (GARCIA-SUCERQUIA et al., 2006) that when the laser-object distance is several thousand times the wavelength used, then the twin image is also very distant from the focused image, thus very unfocused and smeared out over the reconstruction and is not significantly disturbant, given that a screen big enough for the desired resolution is used.

Simplified versions of the Kirchhoff-Helmholtz diffraction formula were proposed by Barton (BARTON, 1988), and later by Kreuzer (KREUZER et al., 1992), the latter being the one implemented in this work.
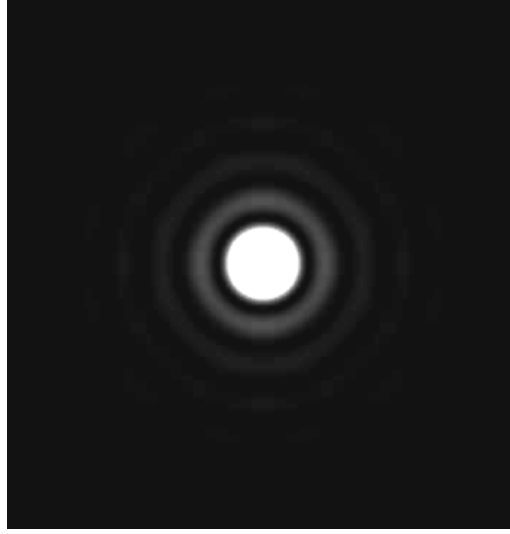
Figure 2.4: The Airy pattern. Levels were adjusted to better illustrate the outer rings.

2.2 Resolution for in-line holographic setups

The model to define the resolution of the system used in this work is based on the diffraction pattern called Airy Pattern, which is the best focused spot of light that a perfect lens with circular aperture can make due to diffraction of light. This pattern is composed by a bright region in the center, the Airy Disk, and a series of concentric bright rings around, as illustrated in Figure 2.4.

Considering this pattern as the best possible focus of a point light source, the resolution of the resulting images can be studied through a model that follows the Rayleigh and the Sparrow criteria for resolution (GARCIA-SUCERQUIA et al., 2006). The former states that two points focused like the Airy Pattern are just resolved when the principal diffraction maximum of one image coincides with the first minimum of the other. In other words, they are resolved when there is a significant dip in intensity between the Airy disks of both points. The latter criteria is less restrictive and states that two Airy disks are just resolved when they are placed closer together until there is no more dip in intensity between them, but no closer, thus they are distinguishable by the elongated shape of the resulting pattern.

It has been demonstrated in (GARCIA-SUCERQUIA et al., 2006) that these criteria are satisfied when the distance between two points d_{ab} satisfies

$$d_{ab} \geq \frac{\lambda}{2NA}, \tag{2.1}$$

where NA is the *numerical aperture* and λ is the wavelength of the radiation being used.

The numerical aperture of a system is a number that represents the range of angles that a system can accept or emit relative to a point position. It is usually defined by $NA = n \sin \theta$, where n is the index of refraction of the medium (*e.g.*, 1.0 in air) and θ is half the angle of the maximum cone of light that can enter or be emitted by the system. This is important for two reasons in the context of this work: the laser diode emits a diverging beam of light that has an elliptical shape, and the smaller diameter of this ellipse at the center of the beam defines the area of light effectively reaching the sensor at a distance, as illustrated in Figure 2.5; and secondly, it is essential in determining the
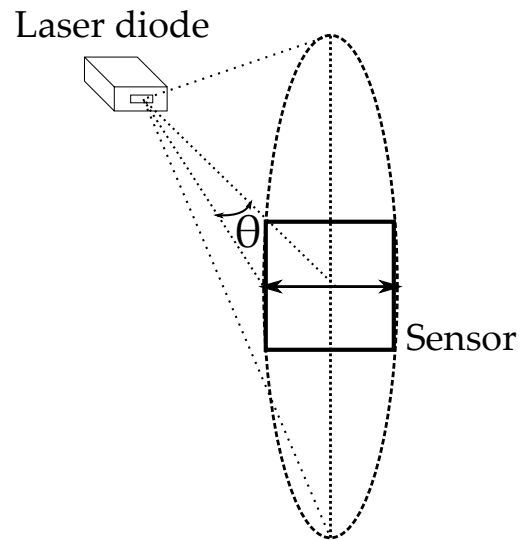
Figure 2.5: Elliptical shape of the laser diode light emission. θ refers to the angle that defines the numerical aperture of the system when using the laser diode.

maximum resolution of a given setup geometry.

3 RELATED WORK

With the goal of overcoming the limitation of lenses in electron microscopy, Gabor introduced holography as a technique to record and reconstruct wavefronts (GABOR, 1948), and in (GABOR, 1949) already featured mathematical means of reconstructing the wavefronts. His arrangement was very simple, with all the elements placed along an axis, as example illustrated in Figure 3.1. The use of a point source of illumination as reference wave provided the desired magnification of the diffraction patterns of the object. This diffraction pattern interferes with the unscattered reference wave and intensity values of this interference are recorded at the screen.

Barton proposed the use of a converging spherical wave to create an image of the original object from a hologram of a similar setup, which is not a practical process, but can be numerically achieved with the Kirchhoff-Helmholtz integral theorem as a means to compute the image intensity of the wave amplitude at any point in the interior of a sphere (BARTON, 1988). Furthermore, he also showed that such a numerical reconstruction could be efficiently performed by Fast Fourier Transforms, with the help of a coordinate transformation.

This approach was given more depth and attention by Kreuzer *et al.* (KREUZER et al., 1992; GARCIA-SUCERQUIA et al., 2006), who used it as a basis for his digital in-line holographic microscopy technique, which is summarized in the next section.

3.1 Digital In-line Holographic Microscopy

Gabor's original in-line arrangement suffered from the fact that the reference wave was in the same optical axis as the object wave. Therefore, the strong reference wave intensity overexposed the much weaker signal from the object wave which were both located in the same area of reconstruction. This problem was addressed by the use of off-axis arrangements, which effectively separated the reference wave from the reconstructed
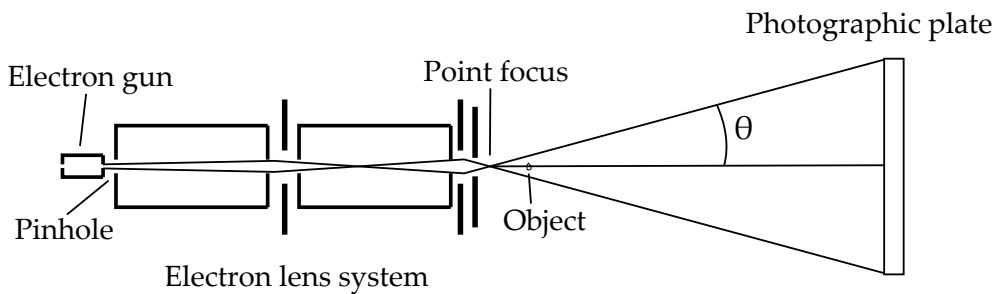
Figure 3.1: Illustration of a setup proposed by Gabor.
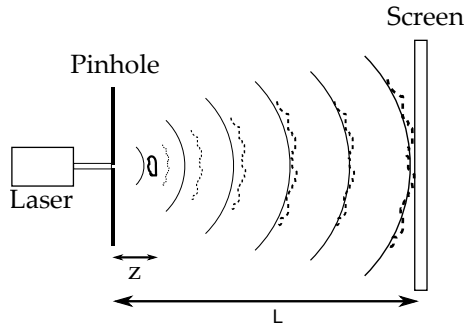
Figure 3.2: Frequently used arrangement in in-line holographic microscopy. Laser is the collimated radiation used; Pinhole refers to the small hole in the order of the wavelength used, in order to create, by diffraction of the collimated light, an spherical wave on the other side; Screen refers to the sensor; z refers to the distance of the object to the point light source (*i.e.*, the Pinhole in this Figure); and L refers to the distance of the Screen to the point light source.

images.

Because we can now record holograms digitally and reconstruct them numerically, the strong background of the reference wave in the in-line setup will not disturb the reconstruction as long as it has weaker intensity variations than the object-related ones. Among other methods, a subtraction of a reference wave recording from the hologram of interest can remove the influence of the reference wave from the reconstruction and is detailed in Chapter 4.

In digital in-line holographic microscopy micrometer resolution can be achieved through a simple setup, comprising in a simple form of an illuminating point source which illuminates an object at a distance and forms a highly magnified diffraction pattern on a screen much farther away, as seen in Figure 3.2. In this kind of setup, the original wave can be considered as divided in two waves: the object wave which is the part of the original wave that was scattered by the object, and the reference wave, which is the part that went through unscattered.

One possible reconstruction algorithm is based on a so-called Kirchhoff-Helmholtz transform detailed in (KREUZER, 2002). This patent describes the manipulation of the integral to a discrete numerical form, which can be computed through Fast Fourier Transforms. The modifications include mainly a coordinate system transform and discretization, and the use of the Bluestein FFT algorithm (BRANDON; BOYD; GOVINDARAJU, 2008) to release the formula from magnification constrains.

Applications of this technique were demonstrated in several contexts, such as biological microscopy (XU et al., 2001), particle (XU et al., 2003) and microorganism tracking (GARCIA-SUCERQUIA et al., 2006), flow analysis (GARCIA-SUCERQUIA et al., 2008). Furthermore, several experimental and theoretical aspects of the process were discussed in (GARCIA-SUCERQUIA et al., 2006).

3.2 Numerically modeling in-line holograms

A very simple way to model in-line holograms was presented in (RESTREPO; GARCIA-SUCERQUIA, 2010). The proposed technique comprises diffraction calculation for an image that represents the object transmittance properties. The necessary equations in one dimension to achieve the result are provided, and details how the Bluestein FFT algorithm

can be used to achieve arbitrary magnifications of the generated patterns.

Although the object representation is essentially flat, the results are quite similar to the holographic patterns that can be observed in in-line setups. Indeed, the same reconstruction algorithm briefly mentioned in the previous section is applicable to the generated images and achieves similar reconstruction images one would expect. This is a very interesting result that opens the possibilities of observing how a particular setup might affect images of particular shapes.

In the next chapter both numerical modeling and reconstruction algorithms are detailed.

4 NUMERICAL IN-LINE HOLOGRAM MODELING AND RE-CONSTRUCTION ALGORITHMS

In this chapter two algorithms are discussed: numerical in-line hologram modeling and reconstruction. The two algorithms have some similarities in the way they use Fourier Transforms, thus a few steps are very similar, although applied to different equations. To facilitate the understanding, these similar steps will be repeated in both algorithms. Both algorithms also features the notion of separate pixels of represented sensors, and the algorithms here discussed assume that each pixel of the represented sensors have equal response to the laser wavelength being used, thus discarding any effect that color filters such as the Bayer filter have upon the response of each pixel. Another important observation is that the algorithms are discussed for monochromatic pixels because the use of the laser dismisses any notion of color and only one wavelength is assumed.

4.1 In-line Hologram Modeling Approach

Numerically modeling in-line hologram images is a good way of analyzing the properties of experimental setups and their effects on the reconstruction, especially in terms of resolution. Restrepo proposed a very simple, yet effective model of in-line holograms for microscopy (RESTREPO; GARCIA-SUCERQUIA, 2010). His model is based on the Fresnel transform, which expresses the propagated interference pattern in a image plane from a reference wave diffracted by a diffracting aperture (*e.g.*, a hologram) in another plane. In his model, the diffracting aperture is an arbitrary image where the complex intensity values means amplitude and phase disturbances, and the image plane is the virtual sensor which will record the intensities of the holographic interference pattern.

The numerically computed amplitude field in one dimension is given in (RESTREPO; GARCIA-SUCERQUIA, 2010), while the two-dimension derivations are presented here. This field $U_{m,n}(z)$, which represents the propagated interference pattern at a distance z, in two dimensions is

$$U_{m,n} = exp\left[\frac{i\pi}{\lambda z}(x_m^2 + y_n^2)\right] \times$$

$$\sum_{p=0}^{N-1}\sum_{q=0}^{N-1} T_{p,q}S_{p,q}\{exp\left[\frac{i\pi}{\lambda z}(\xi_p^2 + \eta_q^2)\right] \times \tag{4.1}$$

$$exp\left[-\frac{i2\pi}{\lambda z}(x_m\xi_p + y_n\eta_q)\right]\},$$

where:

- $U_{m,n}$ is the complex amplitude of the propagated holographic pattern at coordinates (x_m, y_n) and at a distance z from the object plane. $x_m = x_0 + m\Delta x$ and $y_n = y_0 + n\Delta y$, where x_0 and y_0 are the coordinates of the first pixel of this discrete plane (*i.e.*, the first pixel in the virtual sensor) and $\Delta x, \Delta y$ are the pixel spacings in horizontal and vertical directions, respectively;

- $\times$ represents multiplication;

- i indicates an imaginary number;

- λ is the wavelength of the modeled radiation source;

- N is the lateral dimension in pixels of both the modeled sample and virtual sensor;

- $T_{p,q}$ is the transmittance function (*i.e.*, the modeled object image) at coordinates (ξ_p, η_q). $\xi_p = \xi_0 + p\Delta\xi$ and $\eta_q = \eta_0 + q\Delta\eta$, where ξ_0 and η_0 are the coordinates of the first pixel of this discrete plane (*i.e.*, the first object pixel) and $\Delta\xi, \Delta\eta$ are the pixel spacings in horizontal and vertical directions, respectively;

- $S_{p,q}$ is the complex amplitude values of the radiation source (*e.g.*, the modeled laser) at each pixel of the modeled sample image, and thus they have the same coordinates of $T_{p,q}$.

The transmittance function can be a real or complex, depending of the kind of desired object. Real values cause amplitude variations, while the imaginary values causes phase variations. The shape of the sample is arbitrary, but the modeled sample has no depth. Because this function is not periodic and the Fourier transforms involved in this algorithm assumes a periodic signal, a border filter is applied to the image before the calculation is done. This avoids the generation of artifact fringes due to the strong white edge of the images against the assumed black signal outside the borders of the image. This also brings the side effect of slightly reducing the area effectively carrying holographic interference patterns. In the left border, this filter could be defined for each pixel as $p'_{x,y} = p_{x,y}x/width$ if $x < width$, where $p'_{x,y}$ is the new pixel value, $p_{x,y}$ is the old pixel value and $width$ is the width of the desired border filter. The same principle can be applied to the other borders.

The reference radiation in the context of this work is a spherical wave emitted from a point source. A spherical wave diverging from a point source located at (x_R, y_R, z_R) in a object plane (ξ, η, d) can be expressed as (KREIS, 2005)

$$S_{p,q} = E_r e^{i(k\rho_{p,q}+\phi)}$$

where

- E_r is a constant amplitude;

- $\rho = \sqrt{(\xi_p - x_R)^2 + (\eta_q - y_R)^+ (d - z_R)^2}$;

- ϕ is a constant phase shift;

- $k = 2\pi/\lambda$.

The amplitude E_r can be omitted because it only affects global intensity value changes, which will not matter because the output values will be scaled for better contrast. In a similar fashion, the phase term ϕ can also be omitted since the entire phase of the wave is shifted to the same amount and will interfere in the same way (KREIS, 2005). Because the object plane is located centered in the origin in this model, and choosing the point source of the laser position as $(0, 0, z_R)$, the spherical wave complex amplitude at each modeled sample pixel is given by

$$S_{p,q} = e^{ik\sqrt{(\xi_0 + p\Delta\xi)^2 + (\eta_0 + q\Delta\eta) + (z_R)^2}}.$$

Expanding the coordinates components of Eq. (4.1) yields

$$U_{mn} = exp\left[\frac{i\pi}{\lambda z}((x_0 + m\Delta_x)^2 + (y_0 + n\Delta_y)^2)\right] \times$$

$$\sum_{p=0}^{N-1}\sum_{q=0}^{N-1} T_{p,q}S_{p,q}\{exp\left[\frac{i\pi}{\lambda z}((\xi_0 + p\Delta_\xi)^2 + (\eta_0 + q\Delta_\eta)^2)\right] \times$$

$$exp\left[-\frac{i2\pi}{\lambda z}((x_0 + m\Delta_x)(\xi_0 + p\Delta_\xi) + (y_0 + n\Delta_y)(\eta_0 + q\Delta_\eta))\right]\},$$

and after simple manipulations one can express it as

$$U_{mn} = exp\{\frac{i\pi}{\lambda z}((x_0 + m\Delta_x)^2 + (y_0 + n\Delta_y)^2$$

$$+\xi_0^2 + \eta_0^2 - 2x_0\xi_0 - 2m\Delta_x\xi_0 - 2y_0\eta_0 - 2n\Delta_y\eta_0)\}\times$$

$$\sum_{p=0}^{N-1}\sum_{q=0}^{N-1} T_{p,q}S_{p,q}\{exp\left[\frac{i\pi}{\lambda z}(2p\Delta_\xi(\xi_0 - x_0) + p^2\Delta_\xi^2 + 2q\Delta_\eta(\eta_0 - y_0) + q^2\Delta_\eta^2)\right] \times \quad (4.2)$$

$$exp\left[-\frac{i2\pi}{\lambda z}(m\Delta_x p\Delta_\xi + n\Delta_y q\Delta_\eta)\right]\}.$$

Recalling the definition of the Inverse Discrete Fourier Transform

$$F(u, v) = \sum_{x,y}^{N-1} f(x, y)exp(\frac{i2\pi}{N}(ux + vy)),$$

one can observe that Eq. (4.2) can be evaluated by an Inverse FFT transform if the terms inside the summation, with the exception of the last exponential, are seen as a function $f(x, y)$ and express it, omitting the terms outside the summation, as

$$U_{mn} = \sum_{p,q=0}^{N-1} f(x, y)exp\left[\frac{i2\pi}{N}(mp + nq)\right] \qquad if \qquad \Delta_\xi = \frac{\lambda z}{N\Delta_x} \quad and \quad \Delta_\eta = \frac{\lambda z}{N\Delta_y}.$$
$$(4.3)$$

This result from Eq. (4.3) yields a modeled holographic pattern at a fixed size. However, this image typically does not occupy the original size (*i.e.*, $N \times N$), as desired, and cannot be adjusted for size because the object-plane sample spacing is fixed to a static

relation to the sensor pixel spacing. This can be addressed by using the Bluestein FFT Algorithm proposed in (BLUESTEIN, 1970). Details of implementation were presented in (BRANDON; BOYD; GOVINDARAJU, 2008) and Restrepo has used it in (RESTREPO; GARCIA-SUCERQUIA, 2010) for the purpose of achieving arbitrary magnification when modeling in-line holograms. It can be used by introducing two identities:

$$
\begin{aligned}
mp &= \frac{m^2 + p^2 - (m-p)^2}{2}; \\
nq &= \frac{n^2 + q^2 - (n-q)^2}{2}.
\end{aligned}
\tag{4.4}
$$

Then Eq. (4.2) can be manipulated to a convolution form by making the substitutions from Eq. (4.4) and simplifying, yielding

$$
\begin{aligned}
U_{mn} = exp\{&\frac{i\pi}{\lambda z}((x_0 + m\Delta_x)^2 + (y_0 + n\Delta_y)^2 \\
&+\xi_0^2 + \eta_0^2 - 2x_0\xi_0 - 2m\Delta_x\xi_0 - 2y_0\eta_0 - 2n\Delta_y\eta_0)\}\times \\
\sum_{p=0}^{N-1}\sum_{q=0}^{N-1} T_{p,q}S_{p,q}\{&exp\{\frac{i\pi}{\lambda z}(2p\Delta_\xi(\xi_0 - x_0) + p^2\Delta_\xi(\Delta_\xi - \Delta_x) \\
&+2q\Delta_\eta(\eta_0 - y_0) + q^2\Delta_\eta(\Delta_\eta - \Delta_y))\}\times \\
&exp\left[\frac{i\pi}{\lambda z}((m-p)^2 + (n-q)^2))\right]\}
\end{aligned}
\tag{4.5}
$$

One can see that Eq. (4.5) is in a convolution form such as:

$$
(f * g)[u,v] = \sum_{x,y=0}^{N-1} f(x,y)g(u-x, v-y).
$$

Therefore, by invoking the convolution theorem (GOODMAN, 2004) one realizes that the convolution in Eq. (4.5) is equal to multiplying the following Inverse Fourier transformed components and calculating the Fourier transform of the result. The Inverse Fourier transformed components are then defined as follows:

$$
\begin{aligned}
A_{u,v} = \sum_{p,q}^{N-1} \{T_{p,q}S_{p,q}&exp\left[\frac{i\pi}{\lambda z}(2p\Delta_\xi(\xi_0 - x_0) + p^2\Delta_\xi(\Delta_\xi - \Delta_x)\right]\times \\
exp\left[\frac{i\pi}{\lambda z}(2q\Delta_\eta(\eta_0 - y_0)\right. &+ \left. q^2\Delta_\eta(\Delta_\eta - \Delta_y))\right] exp\left[\frac{i2\pi}{N}(up + vq)\right]\},
\end{aligned}
\tag{4.6}
$$

$$
B_u = \sum_{p}^{N-1} exp\left[\frac{i\pi}{\lambda z}\Delta_x\Delta_\xi p^2\right] exp\left[\frac{i2\pi up}{N}\right],
\tag{4.7}
$$

$$
B'_v = \sum_{q}^{N-1} exp\left[\frac{i\pi}{\lambda z}\Delta_y\Delta_\eta q^2\right] exp\left[\frac{i2\pi vq}{N}\right].
\tag{4.8}
$$

Note that if $\Delta_{X'} = \Delta_{Y'}$ is assumed, *i.e.*, the pixel spacings in the sensor are equal in both dimensions, B_u and B'_v is essentially the same component and can be computed just once. Multiplying the three Inverse Fourier transformed components $A_{u,v}$, B_u and B'_v and computing the Fourier transform of the result yields

$$
\begin{aligned}
U_{mn} = exp\{\frac{i\pi}{\lambda z}((x_0 + m\Delta_x)^2 + (y_0 + n\Delta_y)^2 \\
+\xi_0^2 + \eta_0^2 - 2x_0\xi_0 - 2m\Delta_x\xi_0 - 2y_0\eta_0 - 2n\Delta_y\eta_0)\} \times \\
\sum_{u,v=0}^{N-1} A_{u,v}B_uB'_v exp\left[\frac{-i2\pi}{N}(um + vn)\right].
\end{aligned}
\tag{4.9}
$$

This result means that now one can control the size of modeled holographic pattern, which can be set to always fill a target size (*e.g.*, the original $N \times N$ pixels) by using a magnifying factor based on the relation of z/L. Eq. (4.9) can be calculated by taking an Inverse FFT of each of the functions in $A_{u,v}$, B_u and B'_v (mind that they are already expressed as Inverse Fourier transformed), multiplying them point to point, and then taking the FFT of the result. Therefore, fast generation of these numerically modeled holograms can be achieved for any two-dimensional shape of modeled sample. When both dimensions of the summation is of the same size N, one of the one-dimensional transforms can be removed by reusing the same results from the other. Furthermore, because these one-dimensional transforms are not dependant on the actual values of the modeled laser or transmittance function, they can be pre-calculated and reused, and then the algorithm takes only two two-dimensional FFT.

It must be said that the convolution in Eq. (4.9) is not performed over the original $N \times N$ sized array. According to the Bluestein FFT algorithm (BRANDON; BOYD; GOVINDARAJU, 2008), the main component Eq. (4.6) must be zero-padded to a size $M \times M$ and $M \geq 2N - 1$, where $M = 2N$ was chosen in this work. Another requirement is that the one-dimensional components Eq. (4.7) and Eq. (4.8) should also be expanded to size M but in a different manner. First let b_n be the array with the values in (4.7). We want to extend b_n to an array B_n of length M. Then the following relationships are required: $B_0 = b_0$, $B_n = b_{M-n} = b_n$ for $0 > n > N$, and $B_n = 0$ otherwise. The same relationships have to be used with Eq. (4.8).

Since U_{mn} is a complex value, typically one computes the magnitude $|U_{mn}|^2$ to use as a representation of the hologram image recorded at the sensor. For displaying purposes, a normalization process can be performed after the magnitude calculation, and the final pixel could be given by

$$
P_{n,m} = \frac{(|U_{mn}|^2 - min(U_{mn}))255}{max(U_{mn}) - min(U_{mn})},
$$

where $min(U_{mn})$ is the minimal value of all $|U_{mn}|^2$ and $max(U)$ is the maximal value of all $|U_{mn}|^2$. This normalization assumes that the pixels will assume values from 0 to 255.

As noted in (RESTREPO; GARCIA-SUCERQUIA, 2010), the use of the Bluestein FFT algorithm with some magnification values have some side effects in the generated hologram, such as overlapping patterns at the borders, which are still an open problem to be addressed. Nonetheless, much freedom of values is provided by the technique in contrast to the single FFT form.
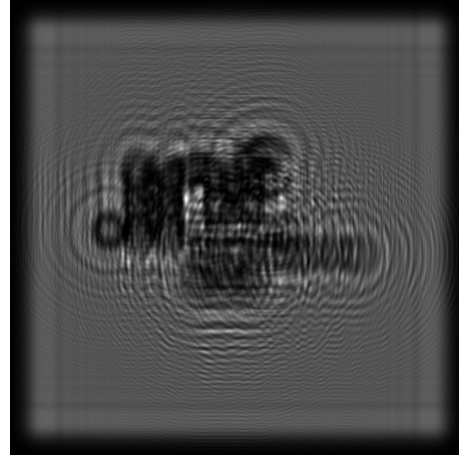
(a) Image used as transmittance function (b) Numerically modeled hologram

Figure 4.1: Example of the calculated holographic pattern with the presented technique

An example of modeled in-line hologram can be seen in Figure 4.1, where one recognizes the characteristic fringes of the holographic interference patterns that one sees in recorded in-line holograms.

The numerical modeling algorithm, which was presented in (RESTREPO; GARCIA-SUCERQUIA, 2010) and here discussed in two dimensions with the border filter and the Bluestein FFT padding techniques presented in (BRANDON; BOYD; GOVINDARAJU, 2008), is summarized below in Figure 4.2.
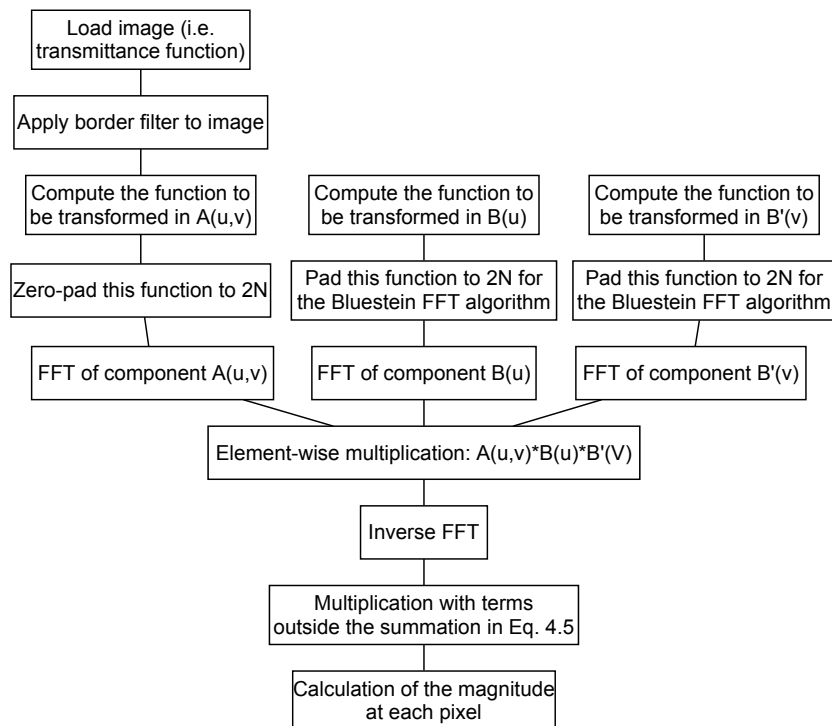

Figure 4.2: Summarized diagram of the hologram modeling algorithm.

4.2 Reconstruction algorithm

In the algorithm proposed in (GARCIA-SUCERQUIA et al., 2006), the first step is to remove as much as possible the reference wave from the hologram. This is done at the recording step, with the laser on, by recording a hologram with and another without the sample present, and then subtracting the latter from the former. The result is a contrast image which is centered around zero intensity and that will eliminate the influence of a d.c.-term in the reconstruction. This process is illustrated in Figure 4.3.

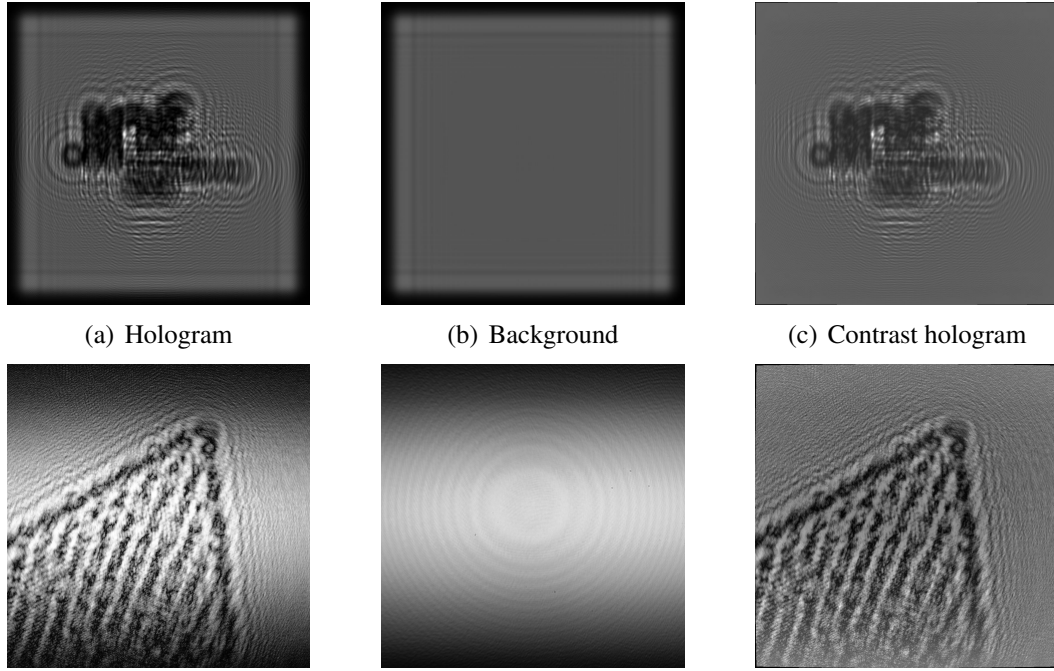| (a) Hologram | (b) Background | (c) Contrast hologram |

Figure 4.3: Removal of the influence of the d.c.-term and reference wave by subtracting an image without the sample present from the hologram. Upper row depicts modeled example while lower row shows captured example. Both contrast images were originally zero-centered, allowing negative intensities, but were shifted to positive values for illustration purposes.

The basis for the reconstruction of in-line holograms in this work relies on the integral theorem of Kirchhoff and Helmholtz, which expresses the optical disturbance in a observation point $K(\vec{r})$ in terms of its values on the surface $Screen$. The reconstruction of the three-dimensional structure from the two-dimensional hologram at the screen can be achieved with a simplified version of the integral theorem, proposed by Barton (BARTON, 1988) and later by Kreuzer (KREUZER et al., 1992). This is called a Kirchhoff-Helmholtz transform and is defined as

$$K(\vec{r}) = \int\int_{Screen} I(\xi)exp(ik\vec{\xi}\cdot\vec{r}/\|\xi\|)d^2\xi \qquad (4.10)$$

where:

- $K(\vec{r})$ is the complex amplitude of the wave modulated by the hologram at position $\vec{r}$;

- $Screen$ is the two dimensional surface of the sensor with coordinates $\xi = (X, Y, L)$, where X and Y are the horizontal and vertical coordinates on the sensor and L is the distance from the source of the laser radiation to the center of the sensor;

- $I(\xi)$ is the contrast image on the sensor obtained by subtracting the image without the sample from the image with the sample present;

- $k = 2\pi/\lambda$ is the wave number of the source of radiation, where λ is the wavelength of the laser;

- i indicates a imaginary number;

- $\vec{r} = (x, y, z)$ is a position vector in the region occupied by the object, where z is the distance of the reconstruction plane distance from the source of the laser, and x, y specifying the location of the reconstructed image in a plane.

The function $K(\vec{r})$ is different from zero and significantly structured only in the space region occupied by the sample (GARCIA-SUCERQUIA et al., 2006). The above formula is not efficient for practical purposes, since it would involve the calculation of the double integral on the entire surface of the sensor for each pixel of the reconstructed plane. Therefore, modifications and manipulations of the Kirchhoff-Helmholtz formula will be now presented to obtain an equivalent formulation which is suited for practical applications of the formula.

A suggestion for implementation was made in (GOLZHAUSER et al., 2002) where Eq. (4.10) is further expanded a coordinate system transform in the values of the sensor as a new screen S' and defined by

$$K(\vec{r}) = \int\int_{S'} I'(X', Y')J(X', Y')exp(ikz\sqrt{1 - X'^2 - Y'^2})exp(ik(xX' + yY'))dX'dY'$$

(4.11)

where:

$$X' = X/\sqrt{X^2 + Y^2 + L^2} \qquad \text{and} \qquad Y' = Y/\sqrt{X^2 + Y^2 + L^2}, \qquad (4.12)$$

$I'(X', Y')$ is the contrast image in the new coordinates, and $J(X', Y') = L^2/(1 - X'^2 - Y'^2)^4$ is the Jacobian.

The following modifications are based on the ones presented by Kreuzer in (KREUZER, 2002), although to a different yet equivalent formulation. Some constant terms outside the summation are omitted, for they affect equally the intensities of all pixels and this is later normalized for displaying purposes. For numerical evaluation, Eq. (4.11) can be expressed in a discrete form by sampling the surface of the sensor as

$$K_{mn} = \sum_{p,q=0}^{N-1} I(X'_p, Y'_q)J(X'_p, Y'_q)exp(ikz\sqrt{1 - X'^2_p - Y'^2_q})exp\left[ik(x_m X'_p + y_n Y'_q)\right]$$

where:

- $x_m = x_0 + m\delta_x$ and $y_n = y_0 + n\delta_n$ are the expanded coordinates on the sample plane, (x_0, y_0) are the first coordinates of the reconstructed plane, and δ_x and δ_y define the sample spacing on the reconstructed plane;

- $X'_p = X'_0 + p\Delta_{X'}$ and $Y'_q = Y'_0 + q\Delta_{Y'}$ are expanded coordinates, where (X'_0, Y'_0) are the first coordinates of the sensor plane (in the new coordinate system) and $\Delta_{X'}$ and $\Delta_{Y'}$ are the sample spacings in the sensor surface on the new coordinates.

Usually one wants to set $\Delta_{X'}$ and $\Delta_{Y'}$ relative to the sensor used in the capture of the hologram. In order to do that, we need to know the first and last positions of the sensor in the original coordinates. For a square sensor centered on the z-axis $X_0 = Y_0 = -H/2 + \Delta_X/2$ and $X_{N-1} = Y_{N-1} = H/2 - \Delta_X/2$, where H is the lateral length of the sensor. Δ_X and Δ_Y are the size of the pixel on the sensor in each direction and in this work they are equal and calculated by $\Delta_X = \Delta_Y = H/N$. In the new coordinates, the following components are defined according to Eq. (4.12):

$$X'_0 = \frac{X_0}{\sqrt{X_0^2 + Y_0^2 + L^2}}; \quad X'_{N-1} = \frac{X_{N-1}}{\sqrt{X_{N-1}^2 + Y_{N-1}^2 + L^2}};$$
$$Y'_0 = \frac{Y_0}{\sqrt{X_0^2 + Y_0^2 + L^2}}; \quad Y'_{N-1} = \frac{Y_{N-1}}{\sqrt{X_{N-1}^2 + Y_{N-1}^2 + L^2}}.$$

With these results the following definitions are obtained:

$$\Delta_{X'} = \frac{X'_{N-1} - X'_0}{N}; \quad \Delta_{Y'} = \frac{Y'_{N-1} - Y'_0}{N}.$$

Expanding the coordinates in Eq. (4.2) yields

$$K_{mn} = \sum_{p,q=0}^{N-1} \{I(X'_p, Y'_q)J(X'_p, Y'_q)exp(ikz\sqrt{1 - (X'_0 + p\Delta_{X'})^2 - (Y'_0 + q\Delta_{Y'})^2}) \times$$
$$exp\left[ik((x_0 + m\delta_x)(X'_0 + p\Delta_{X'}) + (y_0 + n\delta_y)(Y'_0 + q\Delta_{Y'}))\right]\}.$$
$$(4.13)$$

Multiplying the terms in the last exponent of Eq. (4.13) and simplifying yields

$$K_{mn} = exp\left[ik(x_0 X'_0 + m\delta_x X'_0 + y_0 Y'_0 + n\delta_y Y'_0)\right] \times$$
$$\sum_{p,q=0}^{N-1} \{I(X'_p, Y'_q)J(X'_p, Y'_q)exp(ikz\sqrt{1 - (X'_0 + p\Delta_{X'})^2 - (Y'_0 + q\Delta_{Y'})^2}) \times \quad (4.14)$$
$$exp\left[ik(x_0 p\Delta_{X'} + y_0 q\Delta_{Y'})\right] exp\left[ik(p\Delta_{X'}m\delta_x + q\Delta_{Y'}n\delta_y)\right]\}.$$

Again, recalling the definition of the Inverse Discrete Fourier Transform

$$F(u, v) = \sum_{x,y}^{N-1} f(x, y)exp(\frac{i2\pi}{N}(ux + vy)),$$

one can observe that Eq. (4.14) can be evaluated by a Inverse FFT transform if the terms inside the summation, with the exception of the last exponential, are seen as a function $f(x, y)$ and express it, omitting the terms outside the summation, as

$$K_{mn} = \sum_{p,q=0}^{N-1} f(x, y)exp\left[\frac{i2\pi}{N}(mp + nq)\right] \quad \text{if} \quad \delta_x = \frac{\lambda}{N\Delta_{X'}} \quad \text{and} \quad \delta_y = \frac{\lambda}{N\Delta_{Y'}}.$$
$$(4.15)$$

This result from Eq. (4.15) indeed yields a reconstruction image. However, this image is typically very small and cannot be adjusted for size because the reconstruction-plane sample spacing is fixed to a static relation to the sensor pixel spacing. Again, as with the previous algorithm, it is now introduced the substitutions presented in the Bluestein FFT algorithm (BRANDON; BOYD; GOVINDARAJU, 2008).

$$mp = \frac{m^2 + p^2 - (m - p)^2}{2}$$
$$nq = \frac{n^2 + q^2 - (n - q)^2}{2} \tag{4.16}$$

Then Eq. (4.14) can be manipulated to a convolution form by making the substitutions from Eq. (4.16) and simplifying, yielding

$$K_{mn} = exp\left[\frac{i\pi}{\lambda}(\Delta_{X'}\delta_x m^2 + \Delta_{Y'}\delta_y n^2)\right] exp\left[ik(x_0 X_0' + m\delta_x X_0' + y_0 Y_0' + n\delta_y Y_0')\right] \times$$

$$\sum_{p,q=0}^{N-1}\{I(X_p', Y_q')J(X_p', Y_q')exp(ikz\sqrt{1 - (X_0' + p\Delta_{X'})^2 - (Y_0' + q\Delta_{Y'})^2}) \times$$

$$exp\left[ik(x_0 p\Delta_{X'} + y_0 q\Delta_{Y'})\right] exp\left[\frac{i\pi}{\lambda}(\Delta_{X'}\delta_x p^2 + \Delta_{Y'}\delta_y q^2)\right] \times$$

$$exp\left[\frac{-i\pi}{\lambda}(\Delta_{X'}\delta_x(m - p)^2 + \Delta_{Y'}\delta_y(n - q)^2)\right]\}. \tag{4.17}$$

One can see that Eq. (4.17) is in a convolution form such as:

$$(f * g)[u, v] = \sum_{x,y=0}^{N-1} f(x, y)g(u - x, v - y).$$

Therefore, as with the previous algorithm, by invoking the convolution theorem (GOODMAN, 2004) one realizes that the convolution in Eq. (4.17) is equal to multiplying the following Inverse Fourier transformed components and calculating the Fourier transform of the result. The Inverse Fourier transformed components are then defined as follows:

$$A_{u,v} = \sum_{p,q}^{N-1}\{I(X_p', Y_q')J(X_p', Y_q')exp(ikz\sqrt{1 - (X_0' + p\Delta_{X'})^2 - (Y_0' + q\Delta_{Y'})^2}) \times$$

$$exp\left[ik(x_0 p\Delta_{X'} + y_0 q\Delta_{Y'})\right] exp\left[\frac{i\pi}{\lambda}(\Delta_{X'}\delta_x p^2 + \Delta_{Y'}\delta_y q^2)\right] exp\left[\frac{i2\pi}{N}(up + vq)\right]\},$$

$$B_u = \sum_{p}^{N-1} exp\left[\frac{-i\pi}{\lambda}(\Delta_{X'}\delta_x p^2)\}\right] exp\left[\frac{i2\pi up}{N}\right],$$

$$B_v' = \sum_{q}^{N-1} exp\left[\frac{-i\pi}{\lambda}(\Delta_{Y'}\delta_y q^2)\}\right] exp\left[\frac{i2\pi vq}{N}\right].$$

Note that if $\Delta_{X'} = \Delta_{Y'}$ is assumed, *i.e.*, the pixel spacings in the sensor are equal in both dimensions, B_u and B'_v are essentially the same component and can be computed just once. Multiplying the three Inverse Fourier transformed components $A_{u,v}$, B_u and B'_v and computing the Fourier transform of the result yields

$$K_{mn} = exp\left[\frac{i\pi}{\lambda}(\Delta_{X'}\delta_x m^2 + \Delta_{Y'}\delta_y n^2)\right] exp\left[ik(x_0 X'_0 + m\delta_x X'_0 + y_0 Y'_0 + n\delta_y Y'_0)\right] \times$$

$$\sum_{u,v=0}^{N-1} A_{u,v} B_u B'_v exp\left[\frac{-i2\pi}{N}(um + vn)\right].$$

(4.18)

This result means that now one can control the size of the reconstructed image, which can be set to always fill a target size (*e.g.*, the original $N \times N$ pixels) by using a magnifying factor based on the relation of z/L, recalling that z is the reconstruction plane distance from the laser and L is the laser-to-sensor distance. The same considerations about the use of the Bluestein FFT algorithm from the previous section applies here thus padding the components for the Bluestein FFT algorithm should be performed.
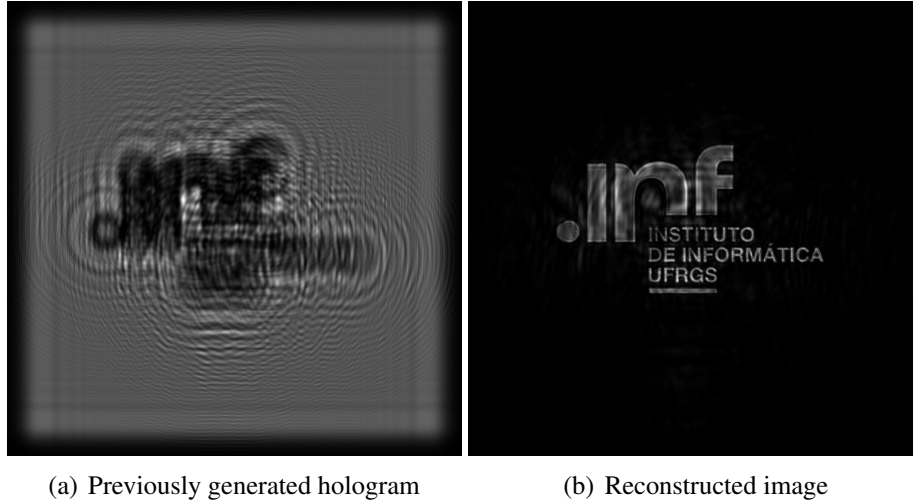

(a) Previously generated hologram   (b) Reconstructed image

Figure 4.4: Example of reconstruction of a hologram with the implemented technique.

Since K_{mn} is a complex value, typically one computes the magnitude $|K_{mn}|^2$ to use as a representation of an image in a given plane between the screen and the point source. For displaying purposes, a normalization process can be performed after the magnitude calculation, and the final pixel could be given by:

$$P_{m,n} = \frac{(|K_{mn}|^2 - min(K_{mn}))255}{max(K_{mn}) - min(K_{mn})}$$

where $min(K_{mn})$ is the minimal value of all $|K_{mn}|^2$ and $max(K)$ is the maximal value of all $|K_{mn}|^2$. This normalization assumes that the pixels will assume values from 0 to 255. A reconstruction example performed by this algorithm can be seen in Figure 4.4.

The numerical reconstruction algorithm, which was presented in (GOLZHAUSER et al., 2002) and here discussed following steps similar as those found in (KREUZER, 2002) with the Bluestein FFT padding techniques of (BRANDON; BOYD; GOVIN-DARAJU, 2008), is summarized below in Figure 4.5.
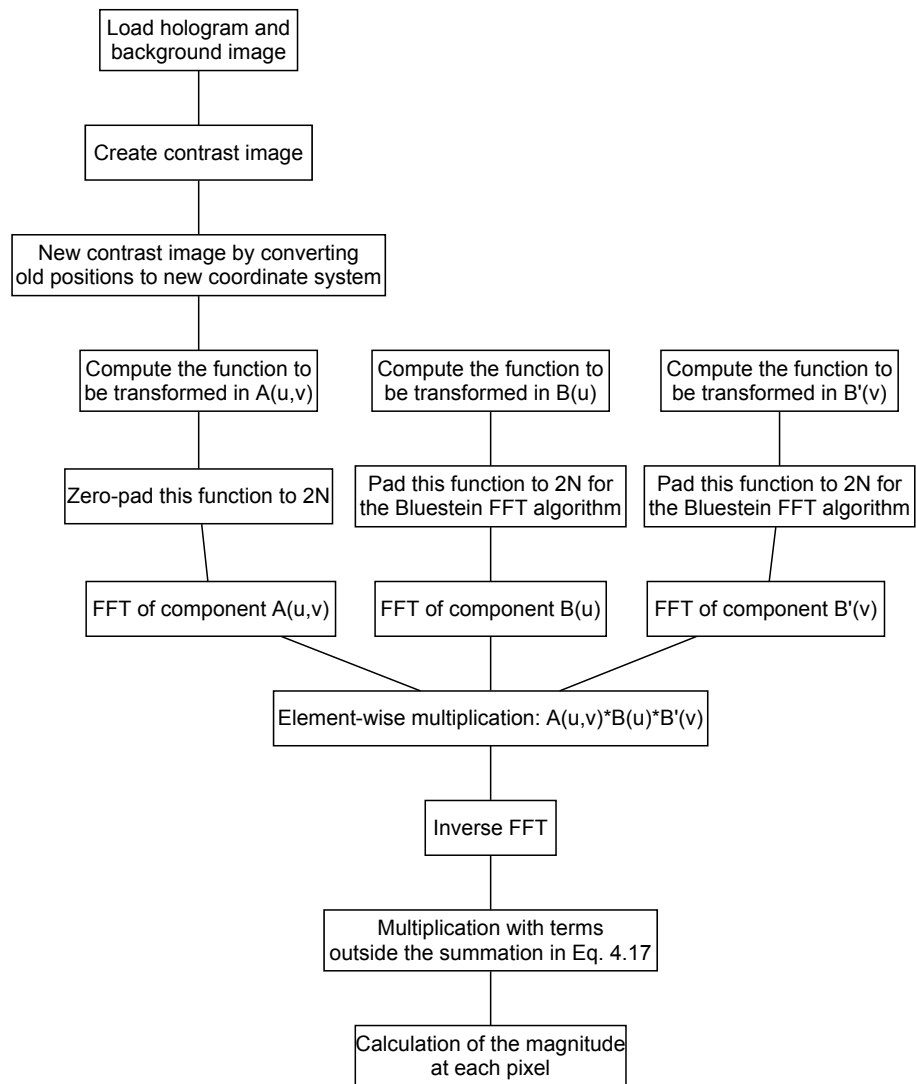
Figure 4.5: Summarized diagram of the reconstruction algorithm.

5   PROPOSED SETUP AND EXPERIMENTAL CONSIDER-ATIONS

In this chapter two setups are proposed for the recording of in-line microscopy holograms. Both of them make use of the laser diode natural divergence as a coherent point source of illumination. One is realized with a Digital Single Lens Reflex (DSLR) camera and the other with a low cost cell phone camera.

5.1   Use of laser diode as point source of coherent illumination

The usual setup for DIHM makes use of components such as laser which produces a collimated beam, a pinhole with size of the order of the wavelength of the laser radiation used and a sensor screen, as illustrated in Figure 3.2. Such a setup requires an accurately sized pinhole, otherwise the laser beam will not reach the other side, or will lose the desired point-source shape and thus will achieve reduced resolution. Another concern in reproducing this setup is the signal-to-noise ratio that comes from the use of the very reduced intensity of the laser radiation that goes through the pinhole and how sensitive is the sensor being used to capture the intensity pattern.

The pinhole itself is also difficult to achieve because of the requirement of its very small aperture which should ideally be sized in the order of the wavelength of the laser (*e.g.*, around $650nm$), but not much larger. Fabricating such a small pinhole is a difficult task to achieve without very accurate tools. The effects of having a bigger than desired pinhole, which allows much of the light to pass collimated and thus losing the spherical wavefront effect has been demonstrated in (GARCIA-SUCERQUIA et al., 2006). Taking these concerns in consideration in terms of cost and other practical matters, the setup used throughout this work is a modified version of the ones commonly used in the literature.

An important modification is the replacement of the collimated laser and pinhole of the original setup for a laser diode extracted from the shell of an extremely low cost red laser pointer, widely available. These laser diodes are similar to a point-source of laser radiation when used without the collimating lens that usually accompanies the diode. However, since the laser diode is not infinitely small, its use as point-source light will have similar effects as a too large pinhole, reducing the achievable resolution. Another concern is that the divergence of the laser is in elliptical shape and the smaller diameter limit the achieved numerical aperture to approximately $NA = 0.11$ as experimentally measured. This was calculated by measuring the size of the beam at a surface placed at a known distance from the laser and applying simple trigonometric relations to find the relation $NA = n \sin \theta$, where θ is the half-angle of the diverging beam and the index of refraction is $n = 1$ for air.

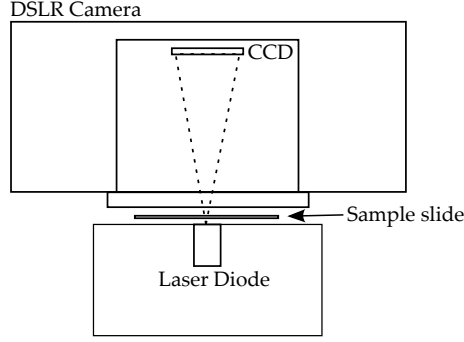DSLR Camera

CCD

Sample slide

Laser Diode

Figure 5.1: Illustration of the DSLR camera prototype arrangement.

Although it is not clear how much directly using the laser diode as illuminating source affects the holographic patterns, the observed fringes and reconstructions seems to imply this does not have great effects on the resolution of the setup other than the reduced numerical aperture. Furthermore, a great benefit of its use is the higher intensity obtained in the recording process, which reduces both the exposure time and the noise level in the sensor. Exposure time is especially important as vibration for such small objects can blur the interference fringes. More importantly, this modification makes the setup so simple that its extremely easy to reproduce.

5.2 DSLR Camera Experimental Setup

The cost of the sensor was also taken into account for the modified setup. Although the resolution of regular consumer cameras could likely be sufficient for this end, they are usually fabricated with undetachable lenses which requires correcting optics to compensate for the possibly unknown optical system. Therefore, the next choice was the use of a Digital Single Lens Reflex camera, which naturally has the possibility of removing its lenses. With this kind of camera, we can expose the CCD array chip by removing the lens or cover of the camera. The DSLR camera used in this work is the Canon EOS 1000D (also known as Canon Rebel XS). This camera has an APS-C Canon format sensor, which is sized at $22.2mm \times 14.8mm$ with 3888×2592 pixels.

As experimentally measured, the laser diode of our tests has a numerical aperture of approximately 0.11 which limits the numerical aperture of the screen when the screen is located at less than 6.88cm from the laser diode. Recalling the resolution equation presented in (GARCIA-SUCERQUIA et al., 2006)

$$d_{ab} \geq \frac{\lambda}{2NA}, \tag{5.1}$$

where $NA = 0.11$ is the numerical aperture and $\lambda = 650nm$ is the laser wavelength for the experimental DSLR setup of this work, we can calculate the maximum achievable resolution which yields approximately $3\mu m$. At this resolution most of the microorganisms and cells will be rendered as small dots of light in the reconstructed image and thus unable to differ them apart from similar-sized particles. However there are interesting subjects that can be captured at this resolution and are shown in Chapter 6. Naturally, interesting possibilities of exploring tracking of these subjects could still be explored.

The recording process used in this setup is quite simple. First a sample is loaded on a regular glass slide and set aside. Then one aligns the center of the laser as much as
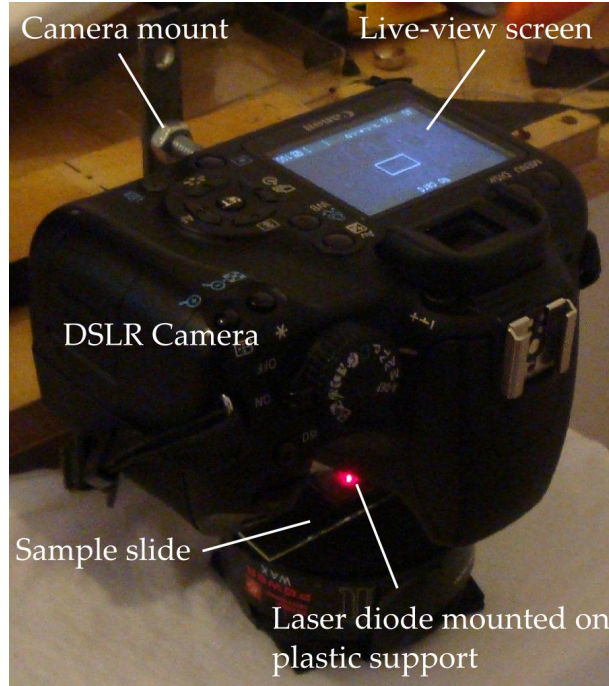
Figure 5.2: Photo of the DSLR camera prototype built for this work.

possible to the center of the sensor. The developed setup makes this very simple because the camera is mounted facing down to the laser which can be freely moved under it. Features such as live-view, which captures real time images of the sensor to a screen and is commonly present in most cameras, help making this alignment a very fast and uncomplicated task. The glass slide is then positioned on top of the laser, at the desired height and one can again use the live-view feature to help finding interesting target patterns to record, much like a regular microscope. High shutter speeds such as $1/1000$ to $1/4000$ of a second can be used when the laser diode is placed near the sensor, *i.e.* around $50mm$. Figure 5.1 illustrates the setup created for this work, while Figure 5.2 shows a photo of the built prototype.

After having performed several experiments with this and slightly different setups, the overall robustness of the in-line holographic process can be observed. Accurate alignment is not necessary for achieving reconstruction for numerical apertures around 0.11. Likewise, one does not need to take accurate measurements of the distances used in the setup because the object can be reconstructed by searching the appropriate distance parameter in the reconstruction step, much like the focusing of a camera. Indeed, it has been demonstrated in (GARCIA-SUCERQUIA et al., 2006) that as long as one sees holographic interference fringes, one gets a reconstruction.

5.3 Low Cost Phone Camera

The second setup is based on a low cost phone camera sensor, along with the same laser diode from the first setup. Unfortunately, cell phone camera sensors are not exposed like that of a DSLR camera, and typically a plastic lens is attached and must be removed. In the case of the cell phone used in this work, a Sony Ericsson W200, the sensor, attached lens and filters formed together a single piece. This had to be carefully broken and cleaned from the debris of this process so that the sensor was exposed as seen in Figure 5.3.

Figure 5.3: Exposed sensor on mentioned low cost cell phone on left and magnified detail on right.

Unfortunately in this particular sensor one can not put the parts together to use as a regular camera again.

The dimensions of the sensor of this phone is not known nor published, and thus from visual assessment it is believed to be close to the $1/6$" format which is $2.3mm \times 1.73$ at 640×480 pixels. The goal of using this setup was mainly to exemplify its use and thus a support apparatus for its use was not developed. Therefore, experimentally recorded images took careful aiming at the desired holographic patterns trying to keep it as stable as possible. Surprisingly, the sensor did adjust reasonably well to the extreme differences of laser intensities and to the unstable recording conditions. Nonetheless, the recorded images still lacked proper background recording and had debris and dust particles on its images, whose effects are commented in Chapter 6.

6 RESULTS

In this chapter two types of experiments are performed in order to observe the various parameters involved in the setups for digital in-line holographic microscopy: numerically modeled scenarios in Section 6.1 and real scenarios in Section 6.2.

6.1 Numerically Modeled Scenarios

Several experiments were designed to observe the influence of the important parameters of any Digital In-Line Holographic Microscope setup. With the help of the modeling application explained in Section 4.1, one can simulate scenarios difficult to experiment with real components. Furthermore, tedious experimental effort is reduced due to precise alignments not being necessary for numerically modeled scenarios, and the focus is shifted to the parameters being observed.

The methodology used in these scenarios is as follows. Instances of the experiment are performed with the parameters being observed changing between them, while the others stay fixed. Naturally some parameters depend on others and these cases are taken into account on the particular experiments. Images of both the numerically modeled holograms and the reconstructions were performed for each instance, although only the reconstructions are shown in most instances for document space reasons. Nevertheless, image quality can be judged visually by the reconstructions alone.

When the following parameters were not particularly being observed, they were kept constant through the experiments: 1024 pixels for lateral resolution, $5.0mm$ for lateral sensor size and 0.11 for numerical aperture.

The image that was used to numerically model the hologram is, as illustrated in Figure 6.1, based on the well-known "1951 USAF resolution test chart" which is still widely accepted as a resolving power test of optical imaging systems such as microscopes.

The following experiments with modeled scenarios were performed and are presented in this section:

- Effects of numerical aperture changes by sensor size variation;

- Effects of numerical aperture changes by laser-to-sensor distance variation;

- Effects of object-to-sensor distance variation

- Effects of sensor resolution variation;

- Effects of laser wavelength variation;

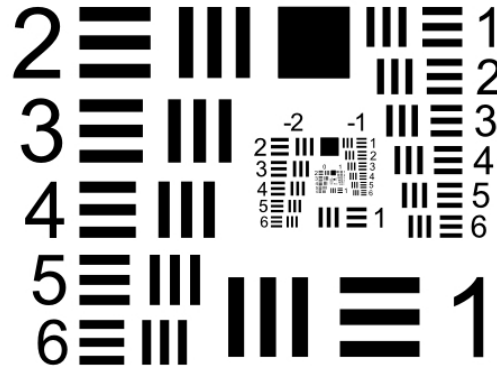- Comparison of commonly available sensor setups.

Figure 6.1: Test image based on the "1951 USAF resolution test chart".
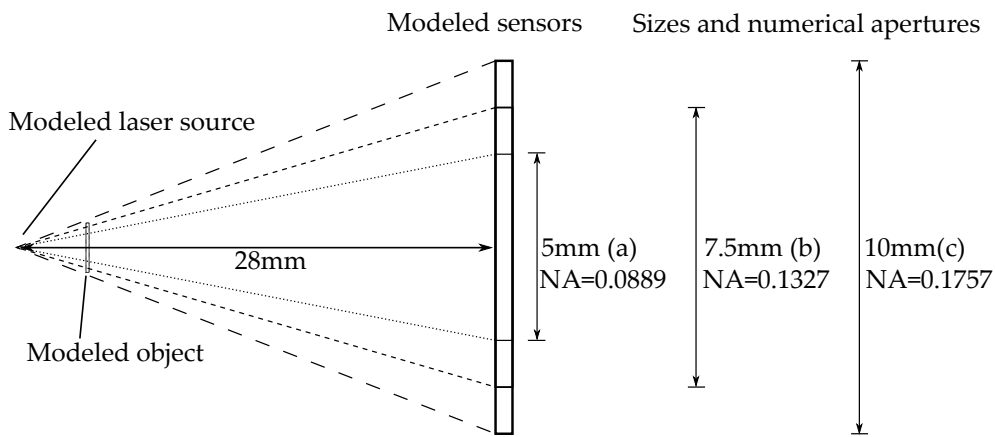

Figure 6.2: Illustration of parameters for observing effects of numerical aperture changes by sensor size variation. The drawn proportions are not related to the actual values.

6.1.1 Effects of numerical aperture changes by sensor size variation

One way to observe the effects of changing the numerical aperture is to modify the sensor size while keeping fixed the distance of the sensor to the point source, as illustrated in Figure 6.2. For geometry reasons, the object plane should change its size accordingly to the sensor size in each instance, which requires extra care when modeling these setups. In essence, all three instances of this comparison have the same test image, but the instances with bigger sensor sizes had their test images padded with transmissive values at the borders instead of just resizing. This is done in order to keep the modeled object (*i.e.*, the modulating black pixels) at the same size in all three instances and thus achieving a consistent comparison.

The change of the numerical aperture and size of the sensor can be noticed by the size of the patterns in the modeled holograms in Figure 6.3, and can also similarly be observed in the reconstructed images of the same figure. For comparison reasons, the reconstructed images in Figure 6.4 were cropped to show the differences in overall resolution of the three instances. It is clear that larger numerical apertures achieved with bigger sensors improve the resolution of the reconstructed images, specially when one desires to achieve high magnification of the object by placing it closer to the point source. When this is done, the holographic patterns will propagate to a bigger area at the sensor and some of the fringes may not be captured, which explains the loss in resolution in this scenario.

The possible effects of keeping or changing the resolution of the sensor in these in-
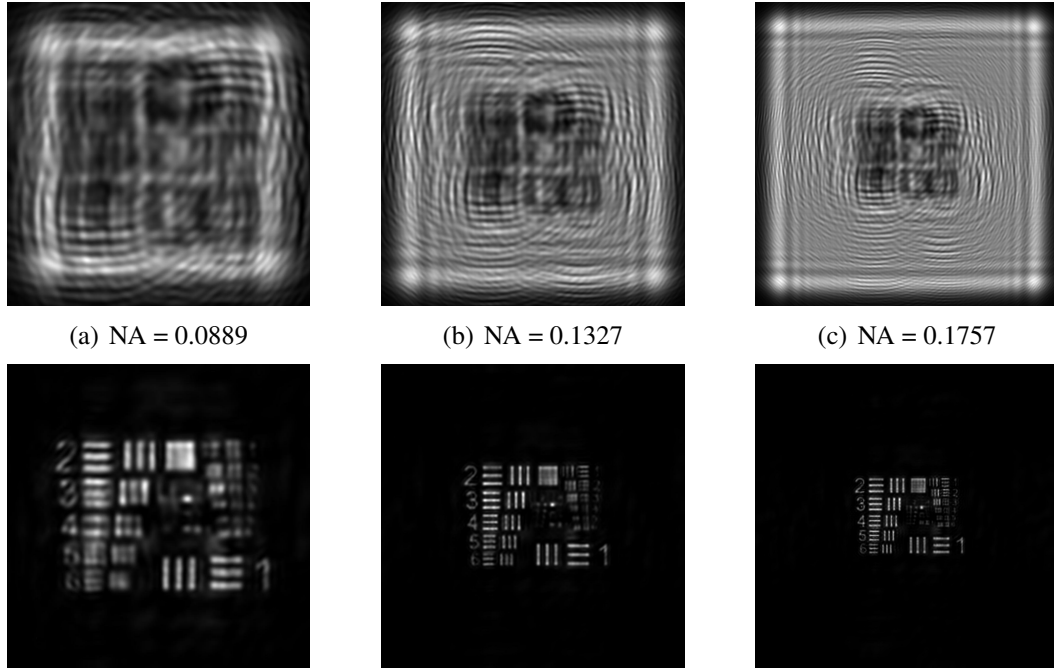
Figure 6.3: Numerical aperture effects on modeled holographic patterns (top row) and resulting reconstructions (bottom row).
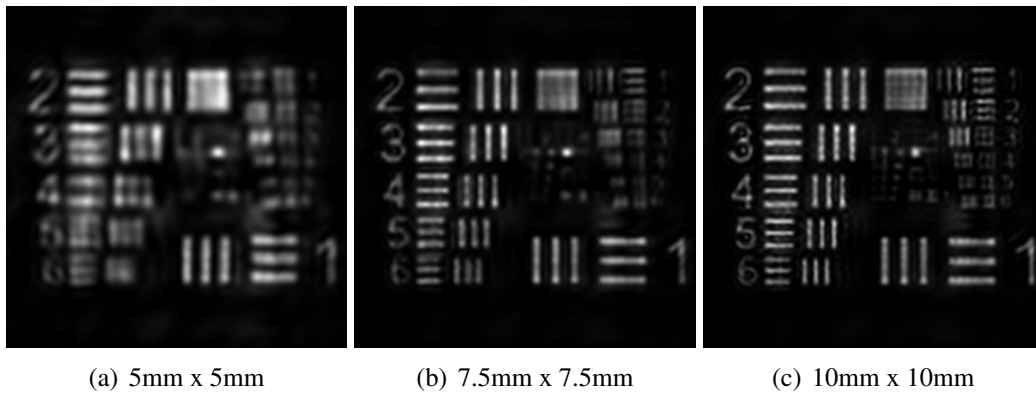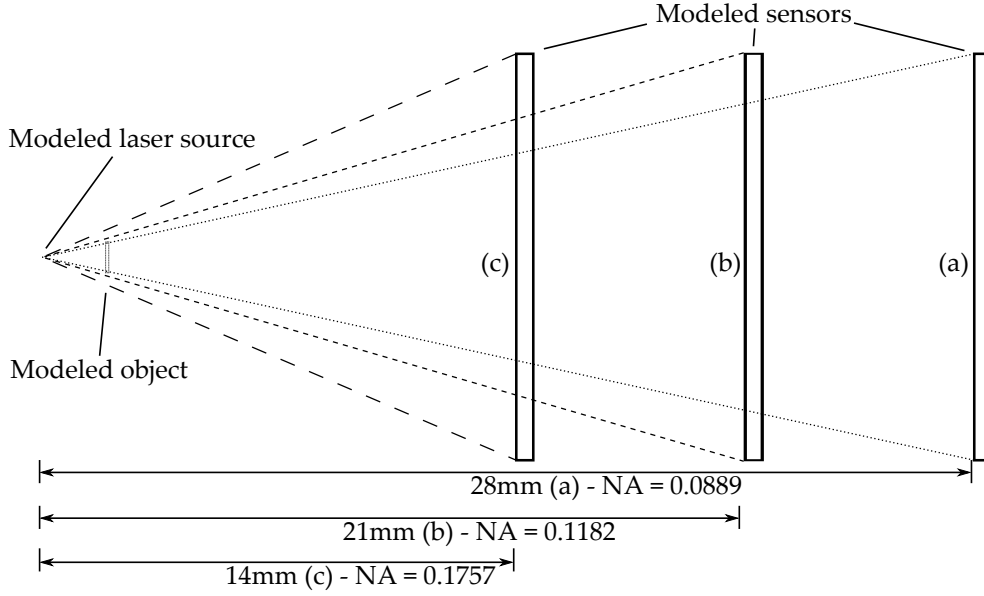

Figure 6.4: Numerical aperture effect by sensor size variation (detail).

stances are similar to the sensor resolution discussion in Subsection 6.1.3.

6.1.2 Effects of numerical aperture change by laser-to-sensor distance variation

Another way to observe the numerical aperture effects on reconstruction quality is to change the sensor distance to the point source laser, while keeping the sensor size fixed. This is illustrated in Figure 6.5. The same care must be taken with the size of the test images to use consistent object sizes, *i.e.*, all three instances of this comparison have the same test image, but the instances with bigger sensor sizes had their test images padded with transmissive values at the borders instead of just resizing.

Similarly to the previous instances, Figure 6.6 shows that larger numerical apertures are related to better reconstruction quality. The reason is again of geometric origin: a sensor closer to the object can capture more interference fringes than at a farther distance.

Figure 6.5: Illustration of parameters for observing effects of numerical aperture changes by laser-to-sensor distance variation. The drawn proportions are not related to the actual values.

(a) 28.0mm   (b) 21.0mm   (c) 14.0mm
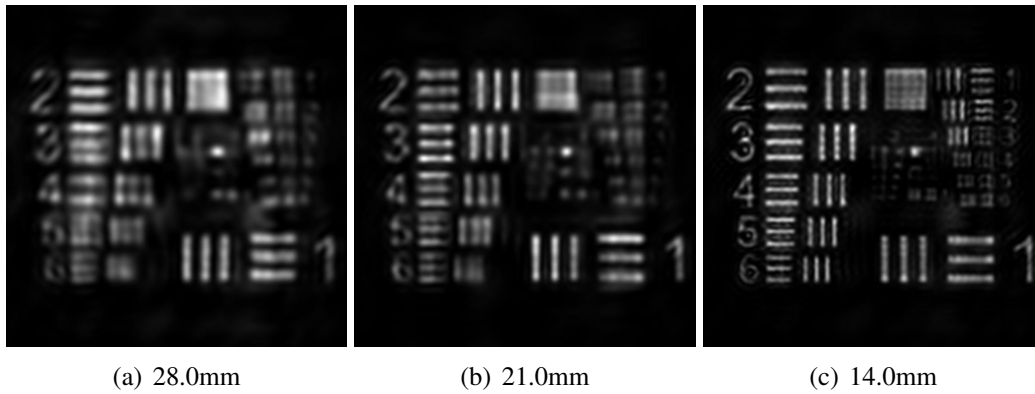
Figure 6.6: Sensor distance effects in hologram reconstruction quality.

6.1.3 Effects of object-to-sensor distance variation

An interesting parameter to observe is the object-to-sensor distance, as illustrated in Figure 6.7. For this experiment, the same care as before must be taken with the size of the test images to use consistent object sizes, *i.e.*, all three instances of this comparison have the same test image, but the instances with bigger sensor sizes had their test images padded with transmissive values at the borders instead of just resizing.

The results from Figure 6.8 seems to imply that object-to-sensor distance has a similar relation as the numerical aperture. By bringing the object closer to the sensor one records more holographic fringes and achieves better resolution. However, it is not clear in the literature how much this parameter affects the resolution limit and what is its relation with the numerical aperture of the system.

6.1.4 Effects of sensor resolution variation

To observe the sensor resolution effects on reconstruction quality a different approach was used. First, a higher resolution modeled hologram was generated, and this one holo-
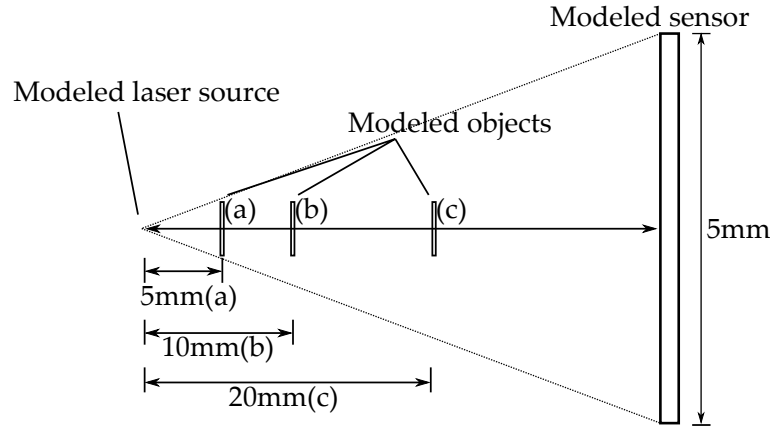
Figure 6.7: Illustration of parameters for observing effects of object-to-sensor distance variation. The drawn proportions are not related to the actual values.

(a) 45mm   (b) 40mm   (c) 30mm
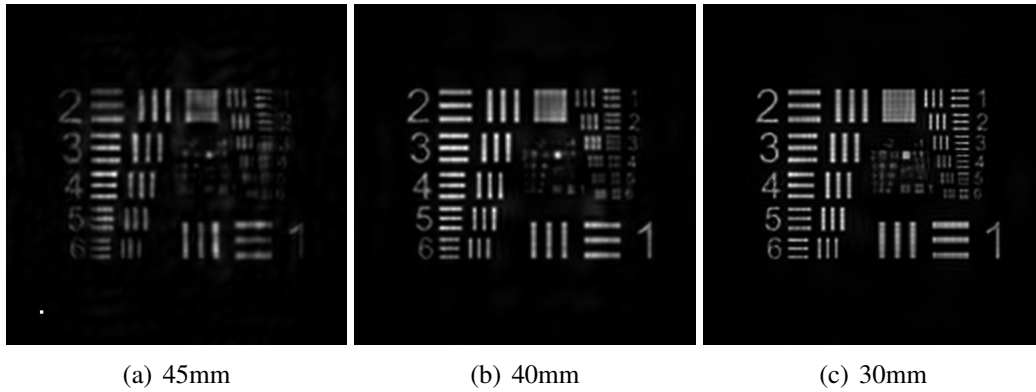
Figure 6.8: Object-to-sensor distance effects on reconstruction quality.

gram was then resized to other smaller sizes in the open-source image editing software Gimp. This software uses a cubic resizing algorithm which in this work is assumed to be a reasonable approximation of sensors with less resolution. This is an effort of simulating how a smaller resolution sensor would detected the incoming higher resolution fringes. These reduced-size images were reconstructed with their own resolution to be compared.

The reconstructions in Figure 6.9 seem to imply that resolution is mainly a quality factor when higher frequency fringes are being recorded. Furthermore, fine detail is lost as expected from lower resolution. Note that this is a very small crop of the reconstruction of the original test image showing only part of the internal group of patterns.The loss of reconstruction resolution due to low sensor resolution is similar to what one would expect of common imagery (*e.g.*, photographs) in that it affects the final results in a similar way. This is in contrast to off-axis holography which produces high-frequency fringes that require high resolution sensors, whereas in DIHM we have relatively low-frequency fringes at high magnifications.

6.1.5 Effects of laser wavelength variation

In the next instance the laser wavelength effects on image quality were observed. In this set, the object was located at 1.0mm from the point source of the laser, which is closer than in the previous sets. The motivation for this is that variations of image quality due to laser wavelength were more pronounced when the object was closer to the laser.

(a) 512 x 512 pixels   (b) 1024 x 1024 pixels   (c) 2048 x 2048 pixels
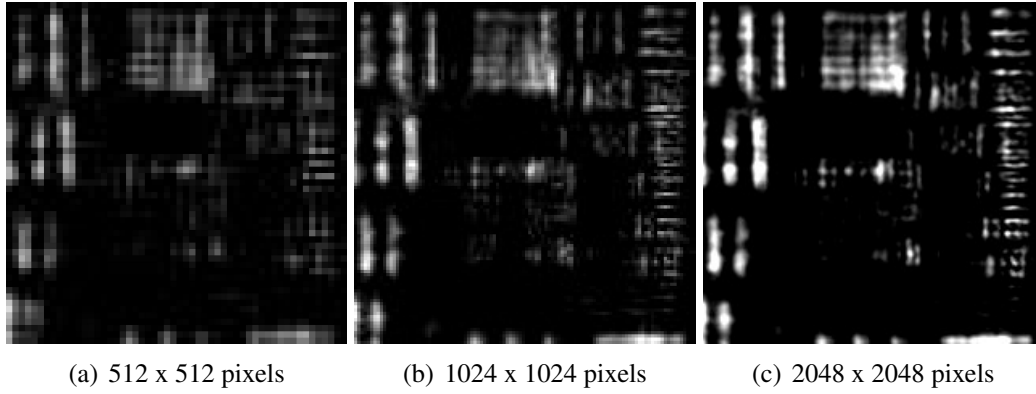
Figure 6.9: Sensor resolution effects in hologram reconstruction quality (very small crop of the center of the pattern). Contrast and brightness enhancements were applied to demonstrate the very subtle difference between the results. These reconstructions show similar difference to expected resolution as in normal images.
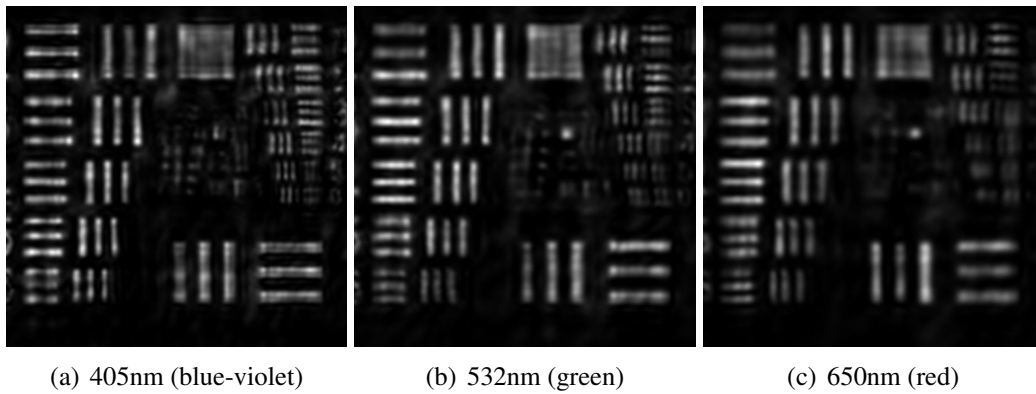

(a) 405nm (blue-violet)   (b) 532nm (green)   (c) 650nm (red)

Figure 6.10: Laser wavelength effects in hologram reconstruction quality (detail excerpt).

As can be seen in Figure 6.10, there is an improvement of image quality when using shorter wavelengths. This result was expected as a consequence of the resolution discussion in Chapter 2, where Eq. (5.1) relates laser wavelength with the numerical aperture of the system. Nonetheless, it is interesting to compare visually what is the actual improvement by using a shorter wavelength.

6.1.6 Comparison of commonly available sensor setups

In order to compare sensors with real specifications such as those from available cameras, a modeled object representing a diatom was generated from an original illustration (ROVAG, 2009). Figure 6.11 depicts one arbitrary species of diatom in a black and white binary image. Diatoms are a major group of algae and are one of the most common types of phytoplankton. To bring it closer to real scenarios, the modeled diatom was assumed to be about $40\mu m$ in length.

The modeled scenarios were based on three different classes of camera sensors: DSLR, point-and-shoot, and low-end cameras (*e.g.*, webcams and cheap phone cameras). These sensor specifications were chosen because they represent a significant part of the available market to end consumers, and similar camera categories would have similar specifications. The modeled DSLR sensor has the common size of the APS-C format from Canon at $14.8mm \times 14.8mm$ and has 2592×2592 pixels, while the point-and-shoot for-
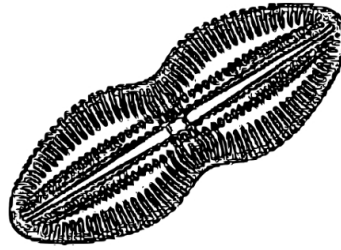
Figure 6.11: Modeled object based on a diatom illustration (ROVAG, 2009).

mat was based on the $1/2.5$" format at $4.29mm \times 4.29mm$ and has 1728×1728 pixels and the one based on the low-end $1/6$" format at $1.73mm \times 1.73mm$ and has 480×480 pixels. Please note that all these sizes and resolutions are based only on the vertical (i.e. smaller) dimensions in order to use square-sized sensor, which is usually the useful area of an captured in-line hologram.

As previously discussed, these results in Table 6.1, Table 6.2 and Table 6.3 reinforce the importance of the numerical aperture in the limit resolution, which brings interesting possibilities of using low-resolution sensors which are now ubiquitous. However, although it is theoretically possible to achieve reasonable numerical apertures with such small sensors, such setups could prove hard to achieve because higher numerical apertures require that small sensors are placed closer to the laser point source.

An interesting result observed in these tables is that sensor resolution is not an important factor for the instances generated with red laser wavelength, and becomes increasingly more important using green laser and shorter wavelengths. Furthermore, even in these shorter wavelengths, only high numerical apertures makes use of the available resolution for details, while for low numerical apertures a low resolution sensor is just as good as the higher one. Furthermore, one could think of systems that aim to achieve tracking of particles with no fine details with a very cheap phone camera and a laser diode.
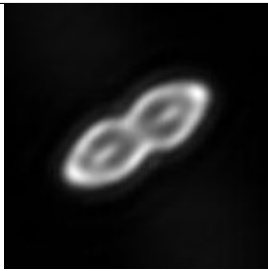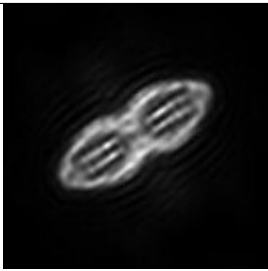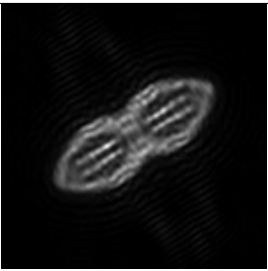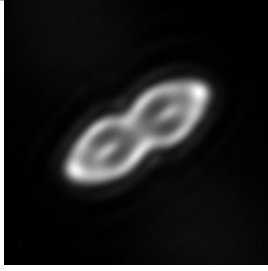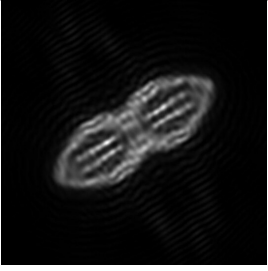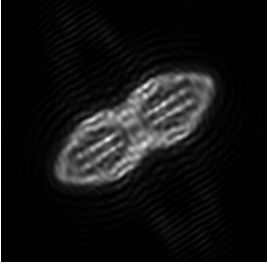
Sensor Spec	NA = 0.11	NA = 0.25	NA = 0.4
1.73mmx1.73mm 480x480 pixels			
4.29mmx4.29mm 1728x1728 pixels			
14.83mmx14.8mm 2592x2592 pixels			

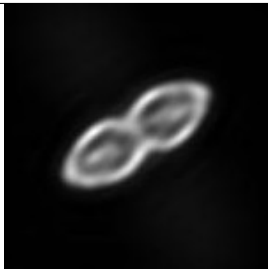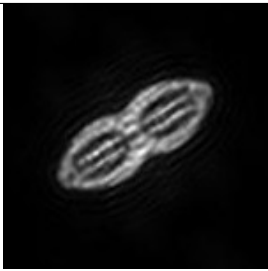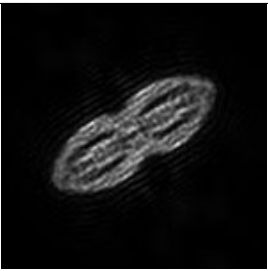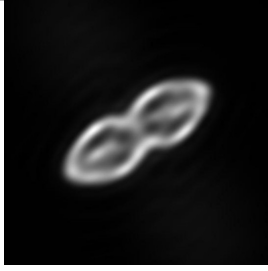Table 6.1: Different setups with red laser wavelength at $650nm$.
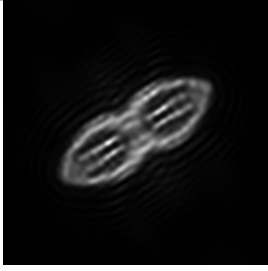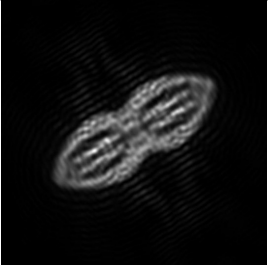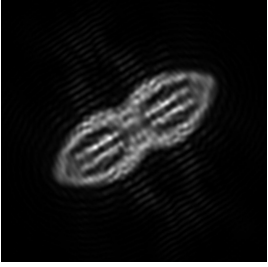
Sensor Spec	NA = 0.11	NA = 0.25	NA = 0.4
1.73mmx1.73mm 480x480 pixels			
4.29mmx4.29mm 1728x1728 pixels			
14.83mmx14.8mm 2592x2592 pixels			

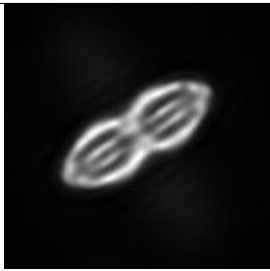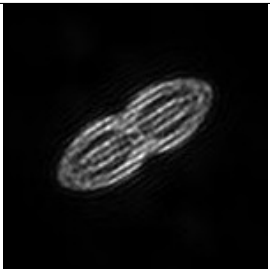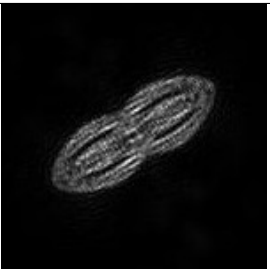Table 6.2: Different setups with green laser wavelength at $532nm$.
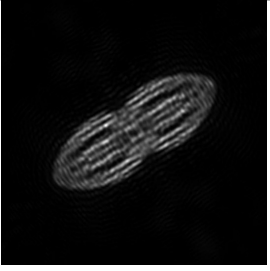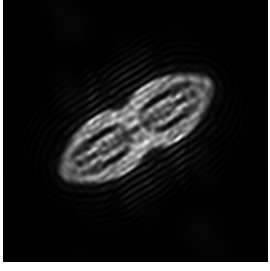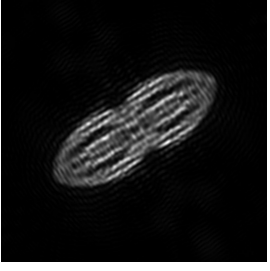
Sensor Spec	NA = 0.11	NA = 0.25	NA = 0.4
1.73mmx1.73mm 480x480 pixels			
4.29mmx4.29mm 1728x1728 pixels			
14.83mmx14.8mm 2592x2592 pixels			

Table 6.3: Different setups with blue-violet laser wavelength at $405nm$.

6.2 Real scenarios

The following experiments were perform with real captured holograms on the DSLR and presented in this section:

- Effects of numerical aperture change by laser-to-sensor distance variation;

- Effects of object-to-laser distance variation.

Furthermore, the use of low cost cell-phone to record in-line microscopic holograms is exemplified in subsection 6.2.2, along with the respective numerical reconstruction.

6.2.1 DSLR setup

In order to observe how the laser to sensor distance affects the recorded and reconstructed holograms, a small layer of onion skin was loaded on a glass slide, which was in turn fixed to the laser at a small distance. This onion skin layer is collected from the inside layers of the onion and looks transparent to the naked eye. The cells are reported to range from $250\mu m$ to $400\mu m$ in length. The reconstructed structures in Figure 6.12 are the cell walls. It should be said that although this onion skin sample is fairly transparent, the ideal sample for in-line holographic microscopy are small objects that let most of the laser go through unscattered. In the case of the onion skin, a better sample would be a smaller cut of the skin with fewer cells.

| (a) 150mm | (b) 100mm | (c) 50mm |

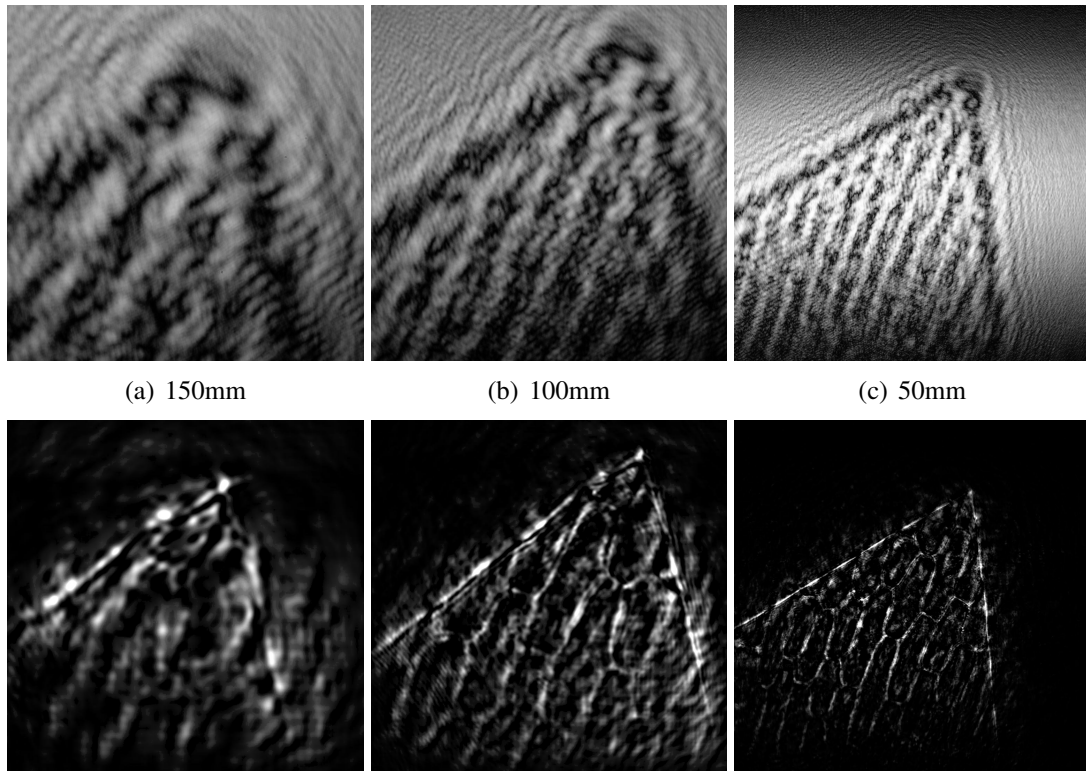Figure 6.12: Laser-to-sensor distance effects on the proposed DSLR setup. The object is a cut onion skin sample. Reconstructed images (bottom row) were enhanced for better contrast, while the holograms (top row) are displayed as recorded.

The results in Figure 6.12 confirm the modeled scenarios effects on sensor distance from the laser. It is clear that closer distances of the sensor to the laser achieves larger
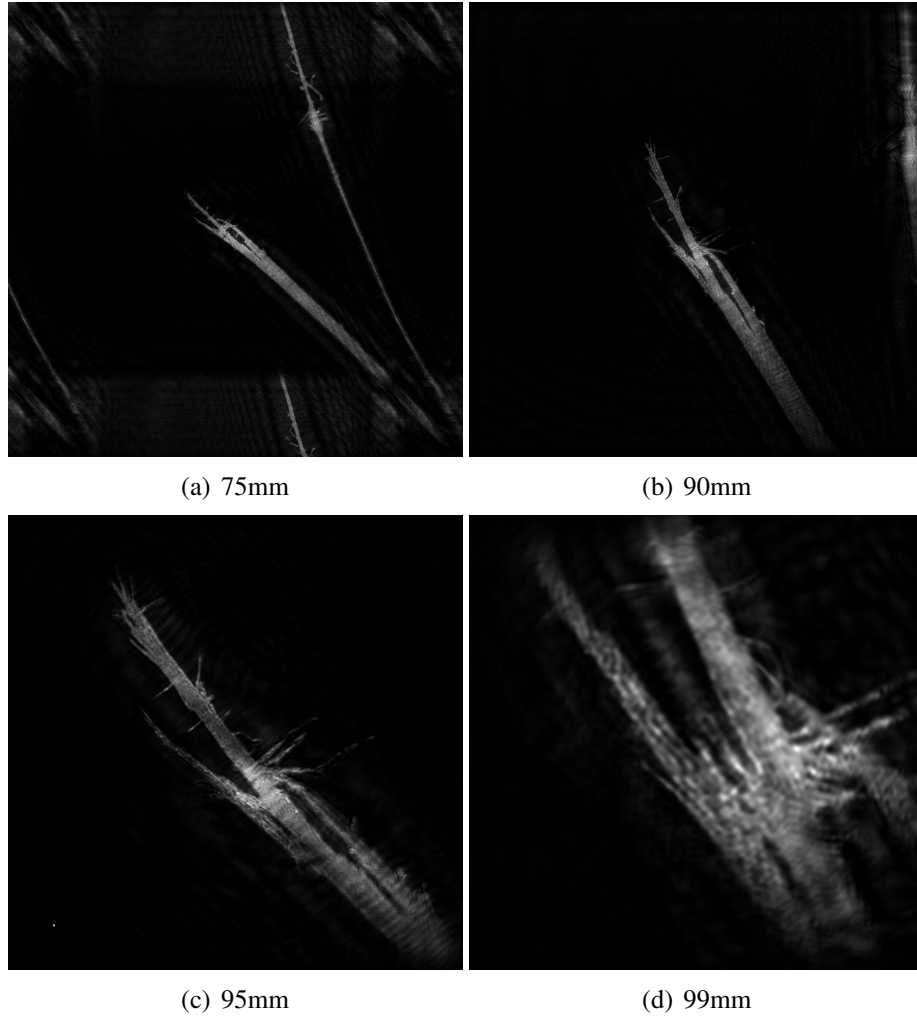
(a) 75mm

(b) 90mm

(c) 95mm

(d) 99mm

Figure 6.13: Object-to-sensor distance effects on the DSLR setup. The object is a split end of an hair strand.

numerical aperture and records more holographic interference fringes, which are lacking in the other two farther away, and thus lower numerical aperture ones. Therefore, while the onion skin cell walls are more clearly defined in Figure 6.12(c), in (b) they are getting fuzzier and in (a) there are almost no shapes present other than the border of the skin sample. Higher resolution versions of Figure 6.12(c) can be found in the appendix Figure A.1 and A.2, in captured hologram form and reconstruction form, respectively. Note that in column (c) of Figure 6.12 the laser diode proximity to the sensor is limiting the area of the sensor that is reached by the beam and has reduced numerical aperture, although still bigger than in the other two instances.

To observe the effects of placing the sample at different distances between fixed laser and sensor, a split end of a hair is used as sample object. A split end of an hair is a usually a damaged part of the hair strand which is divided into two or more strands, and usually features several smaller branches. A human hair has an average width of $90\mu m$, and the details depicted in Figure 6.13 are from one of the divided strands of the hair. The laser to sensor distance was kept fixed at $100mm$ and the split end was moved in between the laser and the sensor for each instance as informed in the captions of Figure 6.12.

Figure 6.13(a) shows the effects of the limitations of the Bluestein FFT algorithm applied to the algorithms in this work, as discussed in Chapter 4. The reconstructed images

in Figure 6.13 depicts the effects of the different placements of the sample between the laser and the sensor, implying that putting the sample too close to laser reduces the overall reconstruction quality, although higher magnification is achieved. Higher resolution versions of Figure 6.13(c) can be found in the appendix Figure A.3 and A.4, in captured hologram form and reconstruction form, respectively.

6.2.2 Low Cost Cell Phone Camera

In order to verify that it is possible to achieve reconstruction of captured images from really low-end sensors such as the ones present in cheap cell phones, a few holograms were taken and one of the reconstructions is presented in Figure 6.14. This is a very promising possibility in that it shows great details of the split end even with such bad experimental conditions. The holograms captured from the phone suffered from unstable experimental conditions and thus the contrast image is obtained through average intensity subtraction instead of background subtraction. This is due to the difficulty of capturing a consistent background, unlike the DSLR setup.

The hologram in Figure 6.14(a) clearly shows some artifacts originated from dust and debris from the modification process previously discussed in Chapter 5. Nevertheless, a reconstruction can be achieved with no perceptible loss in image quality. Although other recorded images from the cell phone do show more artifacts such as saturation, motion blur due to vibration, speckles and debris, the fact that clear holograms can be captured with such simple setups open possibilities for new applications designed for remote location recording and analyzing.
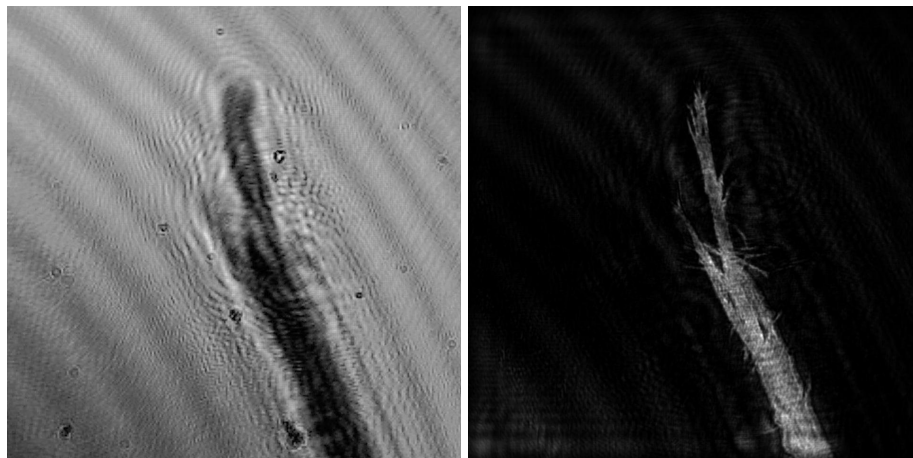
(a) Hologram of a split end of an hair strand captured with low-cost cell phone sensor

(b) Reconstructed image

Figure 6.14: Example of reconstruction of a hologram of a split end of an hair strand captured with low cost cell phone sensor.

7 CONCLUSIONS AND FUTURE WORK

This work presented an analysis of in-line holographic microscopy setups which identified the important parameters of such arrangements. Simulated setups were numerically modeled and reconstructed to verify the effects of changing different setup parameters, such as numerical aperture by sensor size and sensor distance variations, sample distance, sensor resolution and laser wavelength.

The results in this work emphasizes the importance of the numerical aperture in the setups. The size of the reconstruction image is reduced relative to the sensor size when one raises the numerical aperture of the system. However, such smaller images contains more information than a bigger image in a lower numerical aperture setting. This was demonstrated through several comparisons in Chapter 6, and the number of recorded fringes is the biggest factor for the resolution variation in the analysis of this parameter.

Through the use of the experimental setup based on a DSLR camera sensor, the effects of some of the discussed parameters were confirmed and it was revealed that the numerical modeling and reconstruction process can be an efficient way to plan setups for specific samples. It also relates a simple setup with known samples to serve as a reference of the quality that can be achieved with those attributes.

By presenting the use of extremely low cost laser diode that, to the best of my knowledge, is the simplest realization of in-line holographic microscopy setups, one can easily reproduce experiments in this work and experiment with other applications. Therefore, with the proposed setup, a pinhole of the order of the wavelength is not required. The numerical aperture of such a system is relatively low, which restricts the kind of sample that can be visually identified. Nevertheless, it might prove very useful for initial experiments and applications such as particle tracking and counting, which do not require extremely fine resolution. Furthermore, due to the intrinsic numerical aperture achieved, accurate alignments of the elements of the system is not particularly important. The establishment of a reconstruction model for the specific shape of the illuminating laser beam would be an interesting possibility for future works.

The extensive comparison of numerically modeled samples and reconstructions of a diatom suggested that, when high numerical apertures are not being used, low resolution sensor have similar reconstruction quality as sensors with much bigger resolution. Furthermore, sensor size also did not have effects on reconstruction quality on such setups. However, as pointed out, some setups with small sensors might prove hard to achieve with such small element distances. Nonetheless this is a very promising result because small size and low resolution are exactly the attributes of sensors that are available everywhere and have extremely low cost.

This promising possibility was verified by constructing a simple setup with a low cost cell phone sensor by removing the integrated optics and filters. Surprising quality was

achieved with bad recording conditions, although experimentation required more effort to realize because of the unstable nature of the setup. Because one expects to place smaller sensors closer to the light to obtain hight numerical apertures, saturation of the sensor by the strong emission of the laser is a significant issue that must be addressed. The use of neutral density filters could prove useful in this matter to reduce the intensity of the laser emission.

And finally the use of the two discussed algorithms together as a means for numerically testing in-line holographic microscopy setups was demonstrated to be very useful at determining how one can better design a particular setup. By the use of this process, better understanding of how each parameter affects the reconstructed image quality is achieved.

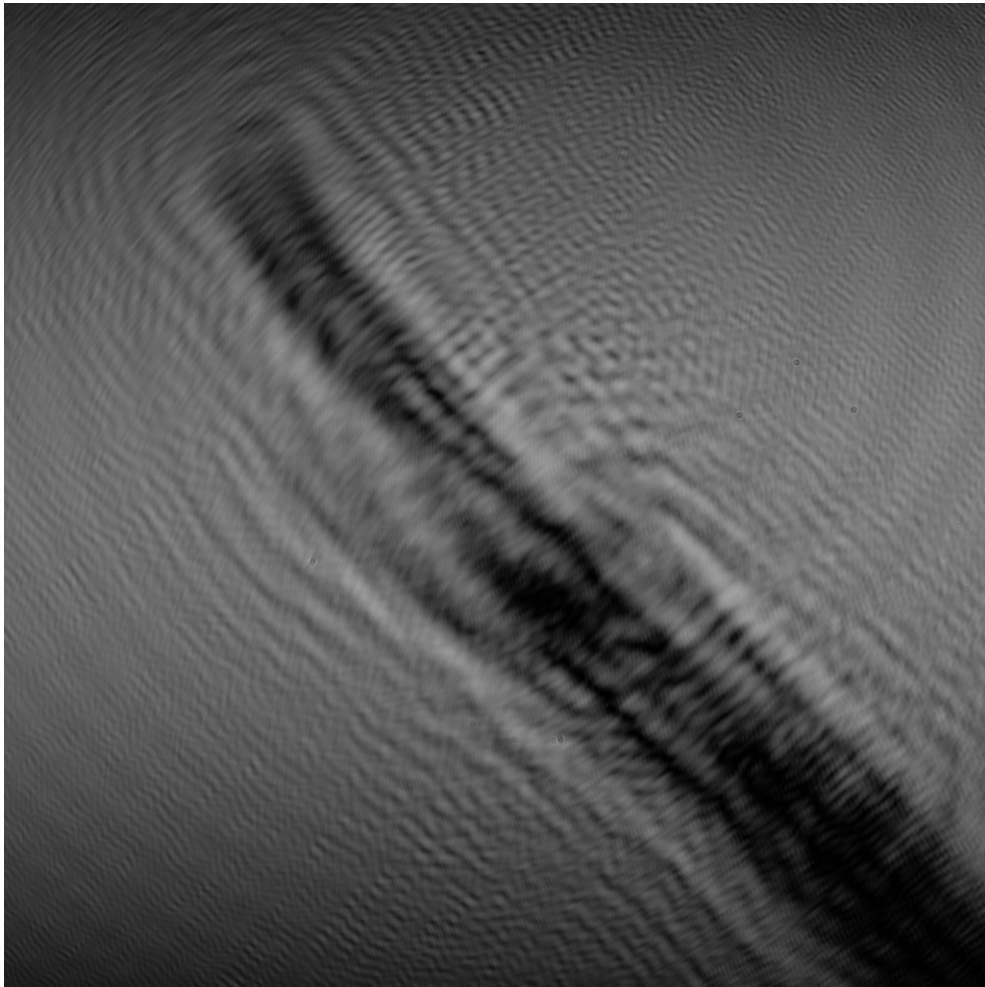# APPENDIX A   EXAMPLES IN HIGHER RESOLUTION
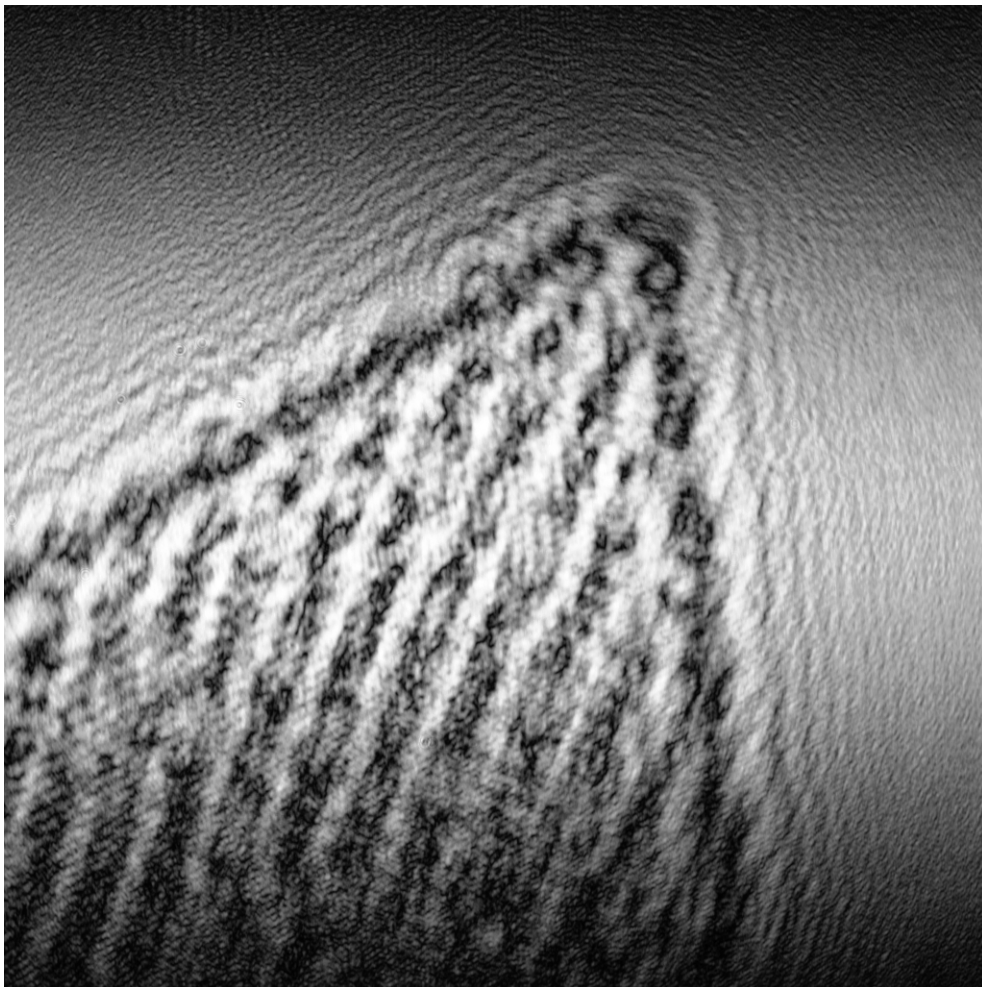
(a) Reconstructed image

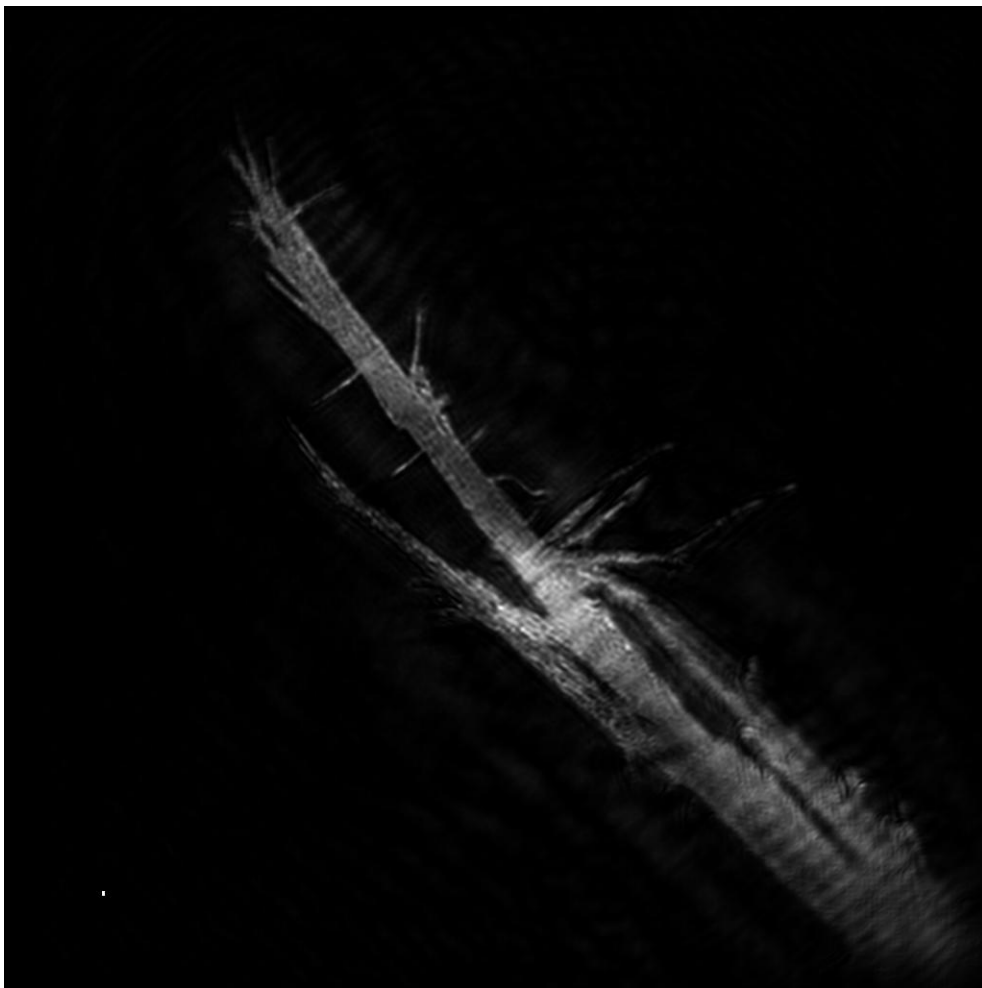Figure A.1: Hologram of onion skin sample captured on the DSLR setup.
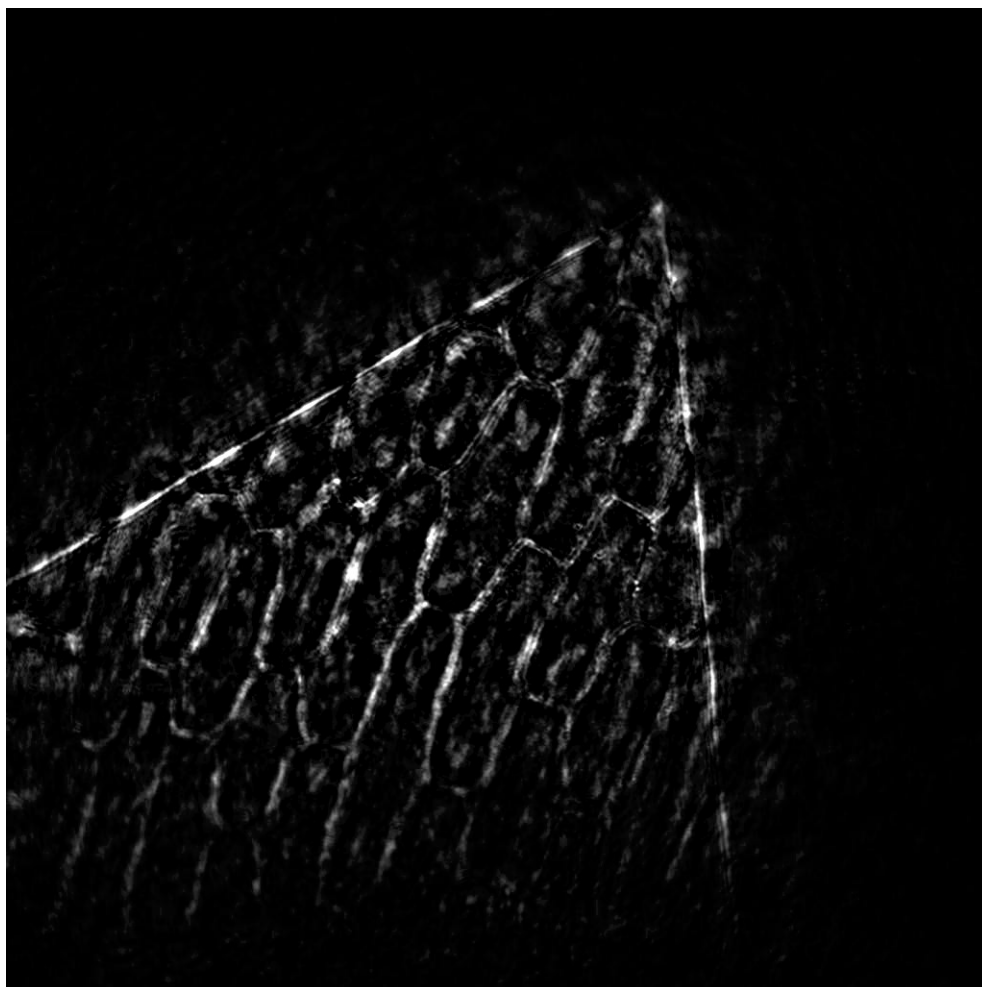
(a) Reconstructed image

Figure A.2: Reconstruction of onion skin sample enhanced for displaying purposes.

(a) Reconstructed image

Figure A.3: Hologram of part of a split end in a hair strand captured on the DSLR setup.

(a) Reconstructed image

Figure A.4: Reconstruction of part of a split end in a hair strand.

REFERENCES

BARTON, J. J. Photoelectron Holography. **Phys. Rev. Lett.**, [S.l.], v.61, n.12, p.1356–1359, Sep 1988.

BLUESTEIN, L. A linear filtering approach to the computation of discrete Fourier transform. **Audio and Electroacoustics, IEEE Transactions on**, [S.l.], v.18, n.4, p.451 – 455, Dec. 1970.

BRANDON, L.; BOYD, C.; GOVINDARAJU, N. Fast computation of general Fourier Transforms on GPUS. In: MULTIMEDIA AND EXPO, 2008 IEEE INTERNATIONAL CONFERENCE ON. **Anais. . .** [S.l.: s.n.], 2008.

GABOR, D. A New Microscopic Principle. **Nature**, [S.l.], v.161, p.777–778, May 1948.

GABOR, D. Microscopy by Reconstructed Wave-Fronts. **Royal Society of London Proceedings Series A**, [S.l.], v.197, p.454–487, July 1949.

GARCIA-SUCERQUIA, J. et al. Digital in-line holographic microscopy. **Appl. Opt.**, [S.l.], v.45, n.5, p.836–850, Feb 2006.

GARCIA-SUCERQUIA, J. et al. 4-D imaging of fluid flow with digital in-line holographic microscopy. **Optik - International Journal for Light and Electron Optics**, [S.l.], v.119, n.9, p.419 – 423, 2008.

GOLZHAUSER, A. et al. Optimization of the low energy electron point source microscope: imaging of macromolecules. **Micron**, [S.l.], v.33, n.3, p.241 – 255, 2002.

GOODMAN, J. W. **Introduction to Fourier Optics**. 3.ed. [S.l.]: Roberts & Company Publishers, 2004.

KREIS, T. **Handbook of Holographic Interferometry: optical and digital methods**. [S.l.]: Wiley-VCH, 2005.

KREUZER, H. et al. Theory of the point source electron microscope. **Ultramicroscopy**, [S.l.], v.45, n.3-4, p.381 – 403, 1992.

KREUZER, H. J. **Holographic microscope and method of hologram reconstruction**. 2002.

RESTREPO, J. F.; GARCIA-SUCERQUIA, J. Modelling High-NA In-Line Holograms. In: BIOMEDICAL OPTICS. **Anais. . .** Optical Society of America, 2010. p.JMA31.

ROVAG. **Diatoms**. `http://commons.wikimedia.org/wiki/File:Diatoms.jpg`.

XU, W. et al. Digital in-line holography for biological applications. **Proceedings of the National Academy of Science**, [S.l.], v.98, p.11301–11305, Sept. 2001.

XU, W. et al. Tracking particles in four dimensions with in-line holographic microscopy. **Opt. Lett.**, [S.l.], v.28, n.3, p.164–166, Feb 2003.